IMAGING IN MOLECULAR DYNAMICS

Technology and Applications
(A User's Guide)

Edited by BENJAMIN J. WHITAKER
Department of Chemistry, University of Leeds, Leeds, UK

CAMBRIDGE
UNIVERSITY PRESS

PUBLISHED BY THE PRESS SYNDICATE OF THE UNIVERSITY OF CAMBRIDGE
The Pitt Building, Trumpington Street, Cambridge, United Kingdom

CAMBRIDGE UNIVERSITY PRESS
The Edinburgh Building, Cambridge CB2 2RU, UK
40 West 20th Street, New York, NY 10011-4211, USA
477 Williamstown Road, Port Melbourne, VIC 3207, Australia
Ruiz de Alarcón 13, 28014 Madrid, Spain
Dock House, The Waterfront, Cape Town 8001, South Africa

http://www.cambridge.org

First published 2003

Printed in the United Kingdom at the University Press, Cambridge

Typeface Times 11/14 pt *System* LaTeX 2_ε [TB]

A catalogue record for this book is available from the British Library

Library of Congress Cataloguing in Publication data

Imaging in molecular dynamics : technology and applications : (a user's guide) / edited by Benjamin Whitaker.
p. cm.
Includes bibliographical references and index.
ISBN 0 521 81059 0
1. Molecular dynamics. 2. Imaging systems in chemistry. I. Whitaker, Benjamin, 1956–
QD461 .I54 2003
541.3'94 – dc21 2002031561

ISBN 0 521 81059 0 hardback

Contents

Contributors

David W. Chandler
Combustion Research Facility, Sandia National Laboratories, Livermore, California, USA.

Alexei I. Chichinin
Institute of Chemical Kinetics and Combustion, 630090, Novosibirsk, Russia.

Tina S. Einfeld
Institut für Physikalische und Theoretische Chemie, Technische Universität Braunschweig, Hans-Sommer-Str. 10, D38106 Braunschweig, Germany.

André T. J. B. Eppink
Department of Molecular and Laser Physics, University of Nijmegen, Toerooiveld 11, 6525 ED, Nijmegen, The Netherlands.

Karl-Heinz Gericke
Institut für Physikalische und Theoretische Chemie, Technische Universität Braunschweig, Hans-Sommer-Str. 10, D38106 Braunschweig, Germany.

Oded Heber
Department of Particle Physics, Weizmann Institute of Science, Rehovot, 76100, Israel.

Hanspeter Helm
Universität Freiburg, Fakultät für Physik. Hermann-Herder-Str. 3, D-79104, Freiburg, Germany.

Paul L. Houston
Department of Chemistry and Chemical Biology, Cornell University, Ithaca, New York, USA.

Theofanis N. Kitsopoulos
Department of Chemistry, University of Crete, 71409, Heraklion, and Institute of Electronic Structure and Laser, Foundation for Research and Technology-Hellas (IESL-FORTH), 711 10 Heraklion, Crete, Greece.

K. Thomas Lorenz
Lawrence Livermore National Laboratory, Livermore, California. USA.

Christof Maul
Institut für Physikalische und Theoretische Chemie, Technische Universität Braunschweig, Hans-Sommer-Str. 10, D38106 Braunschweig, Germany.

Ulrich Müller
Universität Freiburg, Fakultät für Physik Hermann-Herder-Str. 3, D-79104, Freiburg, Germany.

David H. Parker
Department of Molecular and Laser Physics, University of Nijmegen, Toerooiveld 11, 6525 ED, Nijmegen, The Netherlands.

T. Peter Rakitzis
Department of Physics, University of Crete, 710 03 Heraklion, and Institute of Electronic Structure and Laser, Foundation for Research and Technology-Hellas (IESL-FORTH), 711 10 Heraklion, Crete, Greece.

James L. Springfield
Griffith University, Brisbane, Australia.

Daniel Strasser
Department of Particle Physics, Weizmann Institute of Science, Rehovot, 76100, Israel.

Toshinori Suzuki
Graduate Chemical Dynamics Laboratory, RIKEN, Wako 351-0198, Japan and PRESTO, Japan Science and Technology Corporation, Japan.

Elisabeth A. Wade
Combustion Research Facility, Sandia National Laboratories, Livermore, California, USA. (Current address: Department of Chemistry and Physics, Mills College, Oakland, California, USA.)

Benjamin J. Whitaker
Department of Chemistry, University of Leeds, Leeds LS2 9JT, UK.

Shio-Min Wu
Department of Molecular and Laser Physics, University of Nijmegen, Toerooiveld 11, 6525 ED, Nijmegen, The Netherlands.

Daniel Zajfman
Department of Particle Physics, Weizmann Institute of Science, Rehovot, 76100, Israel.

6

3-D Imaging technique – observation of the three-dimensional product momentum distribution

ALEXEI I. CHICHININ, TINA S. EINFELD,
KARL-HEINZ GERICKE AND CHRISTOF MAUL

6.1 Introduction

As we have seen in the previous chapters inversion algorithms are required in conjunction with two-dimensional (2-D) detection methods in order to reconstruct the velocity (speed and angle) distributions of the products of photodissociation processes. Since these generally need to make certain assumptions about the symmetry of the measured distributions it would be desirable to measure the velocity distribution directly by making a simultaneous measurement of the position and arrival time of each of the photoproducts. In the previous chapter we saw how two charge-coupled device (CCD) cameras can be used in conjunction to make such a measurement. The present chapter develops this idea further by describing a newly developed three-dimensional (3-D) photofragment imaging technique. In this context the term '3-D imaging' refers to the simultaneous measurement of all three coordinates of a single particle, which are defined by the spatial position in the 2-D surface of the position-sensitive detector (PSD) and by the time of arrival at the detector (the third dimension) of the ionized product of a photodissociation process. The transverse velocity components (v_x, v_y) of the initial velocity of the product are determined from the measured 2-D impact position on the PSD surface, while the measured time of arrival gives the longitudinal component (v_z) of the velocity. Hereafter the laboratory axes X, Y, and Z are directed along the laser beam, the molecular beam, and the accelerating electric field, respectively (Fig. 6.1). Directly determining the 3-D velocity distribution of the product provides complete information about the photodissociation process. Note that this technique may easily be extended to study the velocity distributions of the products of chemical reactions; a second molecular beam must be added in this case.

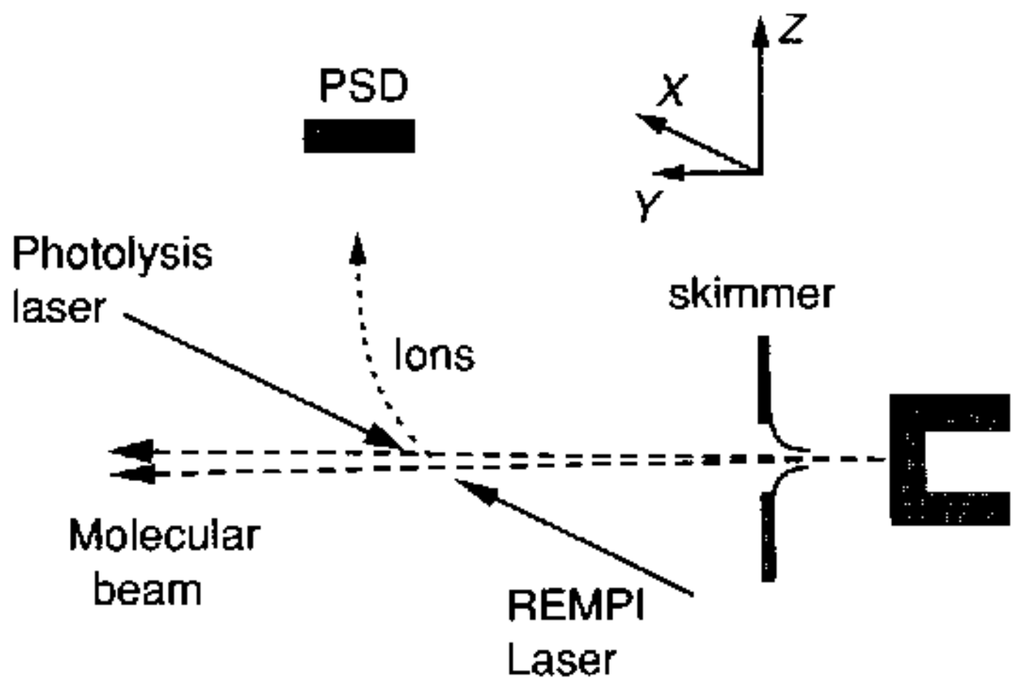

Fig. 6.1. Schematic depiction of the REMPI/TOF mass spectrometer with PSD provided for 3-D photofragment imaging. Also shown is the coordinate system used in this work: the X axis is defined by the laser beam, the Y axis by the molecular beam, and the Z axis by the spectrometer axis.

6.1.1 Why 3-D imaging?

What are the principal advantages of the 3-D imaging techniques over the 2-D 'velocity map imaging' method? As we have seen in Chapter 3 in order to analyse 2-D 'velocity map' images the Abel inversion algorithm or the forward convolution analysis is usually used. The Abel algorithm is rather simple, but it has several limitations: first, it assumes cylindrical symmetry of the initial 3-D distribution, second, the electric field vector **E** of the dissociative radiation must be perpendicular to the Z axis ($\mathbf{E} \perp \mathbf{Z}$), and third, a rather large number of data points is necessary to reconstruct the 3-D distribution of the ions. The forward convolution analysis is more powerful, but it is computationally expensive and, in general, does not lead to unique solutions [1].

In contrast to the 2-D method, the 3-D imaging approach is quite straightforward. Integration techniques, such as the Abel inversion algorithm or the forward convolution analysis, are not required. Moreover, the 3-D imaging approach is more universal: it can be used with any polarization geometry, including the common cases ($\mathbf{E} \parallel \mathbf{Z}$) and ($\mathbf{E} \perp \mathbf{Z}$), and it does not assume any symmetry of the initial 3-D distribution.

There are several phenomena that may break the cylindrical symmetry of the initial fragment distributions. First, alignment of the parent molecules in the cold molecular beam: collisions occurring during the supersonic expansion can produce the molecules in their lowest rovibrational states with alignment of the rotational angular momentum along the axis of the molecular beam [2,3]. The degree of alignment, which can be rather large, varies strongly with the molecular speed, and it is expected to depend on the experimental conditions [2]. The phenomenon has been observed for O_2 [4,5] and N_2 [6] seeded in lighter carriers, for CO seeded in

He [7], and for N_2^+ drifted in He [8]. Evidence for the effect has been also reported for benzene [3]. This effect changes the relative intensities of ions travelling along the Y axis and the X or the Z axis. Second, alignment of the products may occur due to a correlation between the **J** and **v** vectors, where **J** is the rotational angular momentum and **v** is the recoil velocity of the products. The 3-D imaging approach does not remove this effect, but it provides many more possibilities to study it. Third, the length of the spot of the REMPI laser (usually about 1 mm) is small, but not negligible in comparison with the size of the ion distribution over the PSD surface (in the range of a few centimetres). This makes the speed distribution along the X axis wider than that along the Y axis.

Another advantage of the 3-D imaging technique is the possibility it offers to perform coincidence measurements [9–13]: that is, to simultaneously detect two fragments generated in the same elementary process from the same parent molecule. Coincidence measurements are especially important for studying the dynamics of photoinduced three body dissociation [14,15] ($ABC + h\nu \rightarrow A + B + C$) since they simultaneously provide 3-D velocities of two fragments while the 3-D velocity of the third fragment can be calculated from the conservation law for linear momentum.

6.2 Experimental method

A possible experimental arrangement for a 3-D imaging apparatus is shown schematically in Fig. 6.2. It consists of an optical system, a molecular beam, a time-of-flight (TOF) mass spectrometer, and a PSD.

6.2.1 Optical system

The optical system generally comprises two pulsed lasers. The first one is a photolysis laser for the photodissociation of the parent molecule; the second one is a probe (ionizing) laser for the state-selective detection of the neutral photofragment by the REMPI technique. If the wavelength of the second laser is suitable for photolysis, then a single-laser configuration is possible. The probe laser is usually a frequency-doubled dye laser or OPO, pumped by a Nd:YAG laser or by an excimer laser. The radiation with the doubled frequency may be extracted, for example, by a Pellin–Broca prism. A straightforward interpretation of the 3-D PSD image requires the spot of the probe laser to be completely inside the spot of the dissociation laser. Hence, both laser beams must be collinear. The beams may propagate towards each other (Fig. 6.1); or they may propagate in the same direction (Fig. 6.2). In the latter case, another Pellin–Broca prism is used to combine the two individual laser beams to a single laser beam with two wavelengths.

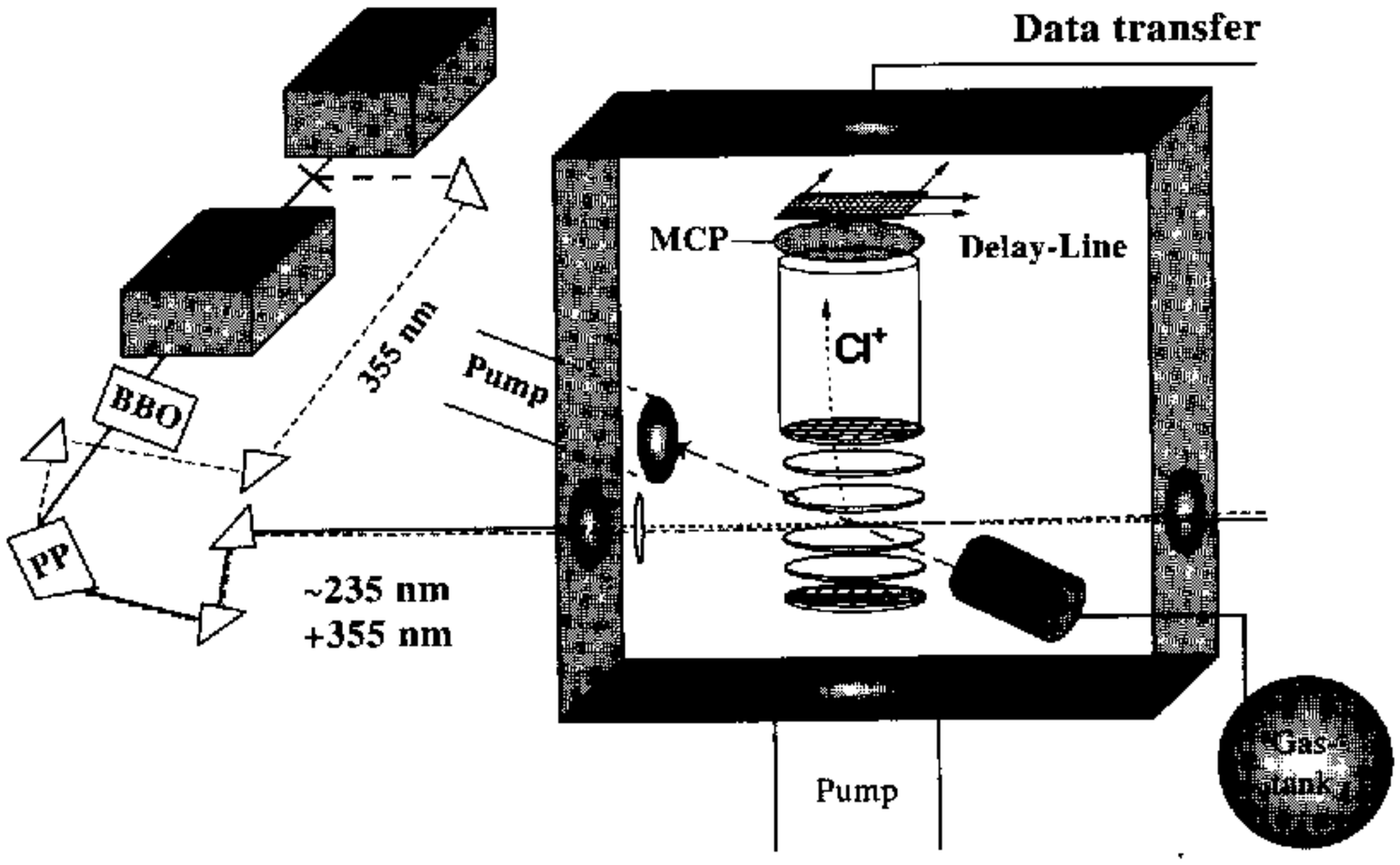

Fig. 6.2. REMPI/TOF/DLD 3-D imaging experimental set-up. PP = Pellin–Broca prism, BBO = frequency-doubling crystal, MCP = micro-channel plate. The photolysis laser is the third-harmonic of a Nd:YAG laser (355 nm), the probe laser is a frequency doubled Nd:YAG laser pumped dye laser. An additional telescope system may be installed on the way of the photolysis laser beam.

Note finally that the adjustment of the optical system and the ion detection system may be rather laborious; hence we recommend the use of a molecular beam with a NO gas mixture for the preliminary alignment because NO molecules in different rotational states may easily be detected by a single-laser set-up with a high sensitivity using a (1 + 1) REMPI scheme via the $A^2\Sigma^+ \leftarrow X\ ^2\Pi$ transition around 226.2 nm [16].

6.2.2 Molecular beam

Although throughout this chapter a cold supersonic continuous molecular beam is assumed, with a few changes the approach may also be used with a pulsed beam. The vacuum system of the TOF mass spectrometer consists of jet and ionization chambers separated by a skimmer (typical diameter of 0.2–0.8 mm). Turbomolecular pumps evacuate both chambers. The molecular beam is obtained by a supersonic expansion of a gas mixture at a pressure of several bar (typically 1–10 bar) through a nozzle. The typical diameter of the nozzle is 10–40 μm: the smaller diameters are difficult in use because they tend to be easily blocked even by very small particles contained in the gas reservoir; the larger diameters require very efficient pumping. It is appropriate to make the distance between the nozzle and the skimmer as large as possible (the larger the distance, the colder the beam), but not larger than the length L_S of the isentropic region termed the 'zone of silence' [17]. The length L_S

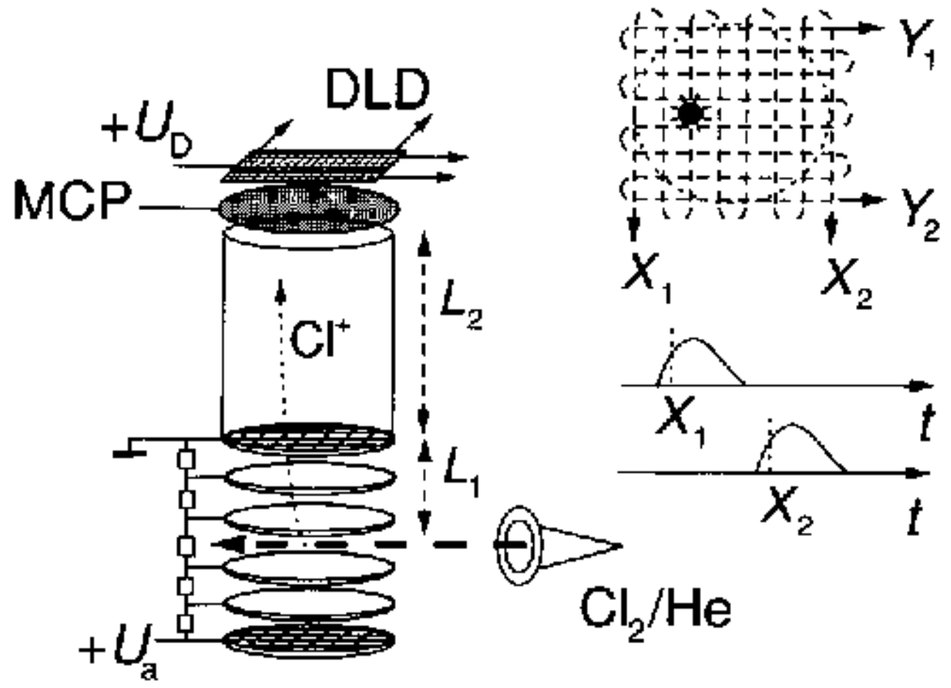

Fig. 6.3. Left: a schematic diagram of the TOF MS. A homogeneous electrostatic field in the acceleration region (L_1) is created by a system of electrode rings. The system is confined by metallic meshes from both sides. Behind the drift region (L_2) the ions impinge upon the MCP. Secondary electrons from the MCP are accelerated towards the DLD. Right: illustration of the DLD principle. Every event generates four signals on the DLD: one on every end of the two orthogonal delay lines, denoted X_1, X_2, Y_1, and Y_2. X and Y coordinates are obtained from the differences $X_2 - X_1$ and $Y_2 - Y_1$, respectively.

is given by $L_S = 0.67\ d\ (P_0/P_b)^{1/2}$, where d is the diameter of the nozzle, P_0 is the initial pressure inside the nozzle and P_b is the background pressure in the jet chamber (typically 10^{-7}–10^{-10} bar). L_S ranges typically from a few centimetres to a few metres, depending on the experimental conditions.

6.2.3 TOF mass spectrometer

In the ionization chamber the skimmed molecular beam is intersected by the probe and the photolysis laser beams whose propagation direction (X axis) is perpendicular to the molecular beam propagation axis (Y axis). The ionization chamber is shown in Fig. 6.3. Products generated in the photodissociation are state-selectively ionized by the probe laser and are accelerated along the Z axis towards the field-free drift region of the TOF MS. Typically, electric field strengths of 3000 V/m are realized by applying an acceleration voltage of $U_a \approx 300$ V to the accelcration stage. The space-focusing condition $2L_1 = L_2$ should be obeyed in order to simplify the interpretation of the 3-D PSD images. Here, L_1 is the length of the acceleration region and L_2 is the length of the drift region (Fig. 6.3). Single ions are detected by a micro-channel plate (MCP) assembly (typical diameters of 4–8 cm). Subsequently, the resulting secondary electrons are monitored by the PSD.

6.2.4 Delay-line position-sensitive detector

In this section we describe the special case of a PSD, which we call a delay-line detector (DLD). The DLD consists of a delay-line anode introduced into the

ionization chamber right behind the MCP assembly (Fig. 6.3). An additional potential ($U_D \approx 300$ V) applied between the MCP and the DLD accelerates the electrons to the delay-line anode. Note that the MCP signal itself, produced by incoming ions and picked up from the charging circuit of the MCP assembly, is only used for adjustment purposes and for the measurement of the mean TOF averaged over all observed single ion events, whereas all quantitative information on the 3-D velocity components of each individual ion is obtained from the DLD signal.

The idea behind a DLD is the following: a signal induced somewhere on a delay line (basically nothing more than a long wire) propagates in both directions towards the ends of the line where impedance adjusted circuits pick it up for further processing (Fig. 6.3). By measuring the time period between the signal arrival times at both ends of the delay line one can determine the position of the signal source along the delay line.

The technical realization of the DLD employed here is described in detail in Refs [18–20]. Briefly, it consists of two individual delay lines oriented orthogonal to each other, thus forming the X–Y plane (Fig. 6.4). A metal body supports ceramic rods placed on the edges; and the delay lines are wound helically on this $8 \times 8\,cm^2$ supporting plate. By this folding technique, a propagation delay of 20 ns/cm and a total single-pass delay of 150 ns is realized, corresponding to a physical length of the delay line of 45 m. Each delay line consists of a pair of wires wound parallel to each other, with a small potential difference (~ 30 V) applied between the two wires of each pair. Thus, the incoming charge cloud from the MCP induces a differential signal on each delay-line pair that propagates to the delay line ends where it is picked up by a differential amplifier.

6.2.5 DLD data analysis

The output charge from the MCP resulting from each single incoming ion or photon ('event') produces altogether four differential signals, two on each delay-line pair

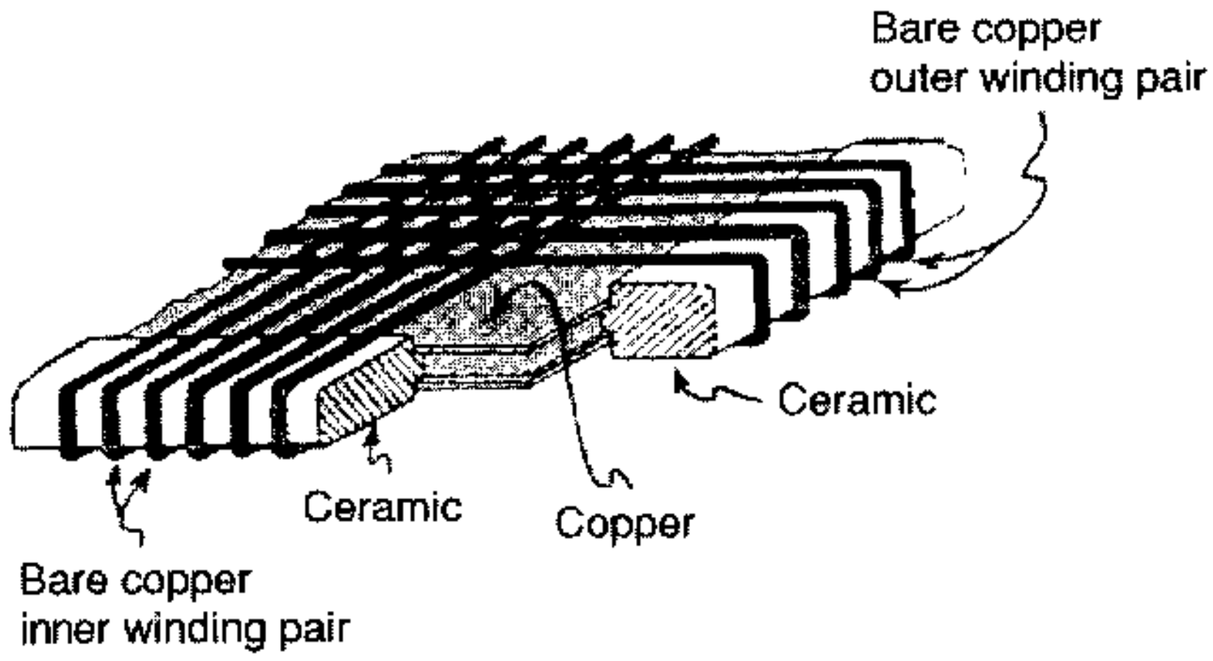

Fig. 6.4. Detail of a helical wire delay-line anode.

(Fig. 6.3). These signals are decoupled from the DC voltages on the wires, amplified, and transmitted to constant fraction discriminators and then to time-to-digital converters. Finally, one event produces two pairs of times, t_{X_1}, t_{X_2} and t_{Y_1}, t_{Y_2} on the delay lines that are wound along the X axis and the Y axis, respectively. The X and Y coordinates of a single event in time units may be calculated as $(t_{X_1} - t_{X_2}, t_{Y_1} - t_{Y_2})$ and the time of the event (corresponding to the Z coordinate) may be calculated as either $(t_{X_1} + t_{X_2})/2$ or $(t_{Y_1} + t_{Y_2})/2$. Thus, the DLD yields the 3-D coordinates of each single event.

The latter condition makes it possible to distinguish between true and false events: the event time provided by the different delay lines must coincide, hence $t_{X_1} + t_{X_2} = t_{Y_1} + t_{Y_2}$. Only those events that obey this condition are counted, and all others are ignored. If more than one ion per laser pulse strikes the MCP assembly, then each delay line produces a series of pulses and the criterion $t_{X_1} + t_{X_2} = t_{Y_1} + t_{Y_2}$ allows one to correctly assign individual pulses to individual ions.

6.2.6 Time and space resolution of the spectrometer

The space resolution of the REMPI/TOF/DLD spectrometer may be determined by experiments with a fine metallic mesh placed just in front of the MCP assembly, which is irradiated by α particles. The wires of the mesh appear as a geometric projection on the DLD, and the dimensions of the wires and the holes of the mesh allow one to determine the spatial resolution of the detector. The image of such a mesh on our DLD is shown in Fig. 6.5. From the analysis of the image one obtains a space resolution of the DLD, which can be better than 100 μm [19]. In the present experiment, the resolution was 400 μm, which still corresponds to a spatial resolution of 1 part in 200 because of the detector size of 80 mm diameter.

The DLD provides the possibility of detecting several products per laser shot, provided a minimal difference between arrival times of 17 ns is maintained. This detector dead time is mainly determined by the typical duration of the pulses on the delay lines. The time resolution for the time of an individual event in the REMPI/TOF/DLD spectrometer is usually limited by the duration of the probe laser pulse, which is of the order of 3–5 ns if a Nd:YAG pump laser is used.

6.2.7 Why DLD?

As has been described in previous chapters the common PSD for a velocity mapping experiment uses a phosphor screen as an optically collecting anode combined with read-out by video camera and/or charge-coupled device (CCD) camera [1,21]. This 'classical' method is optimized for the 2-D imaging of single particles.

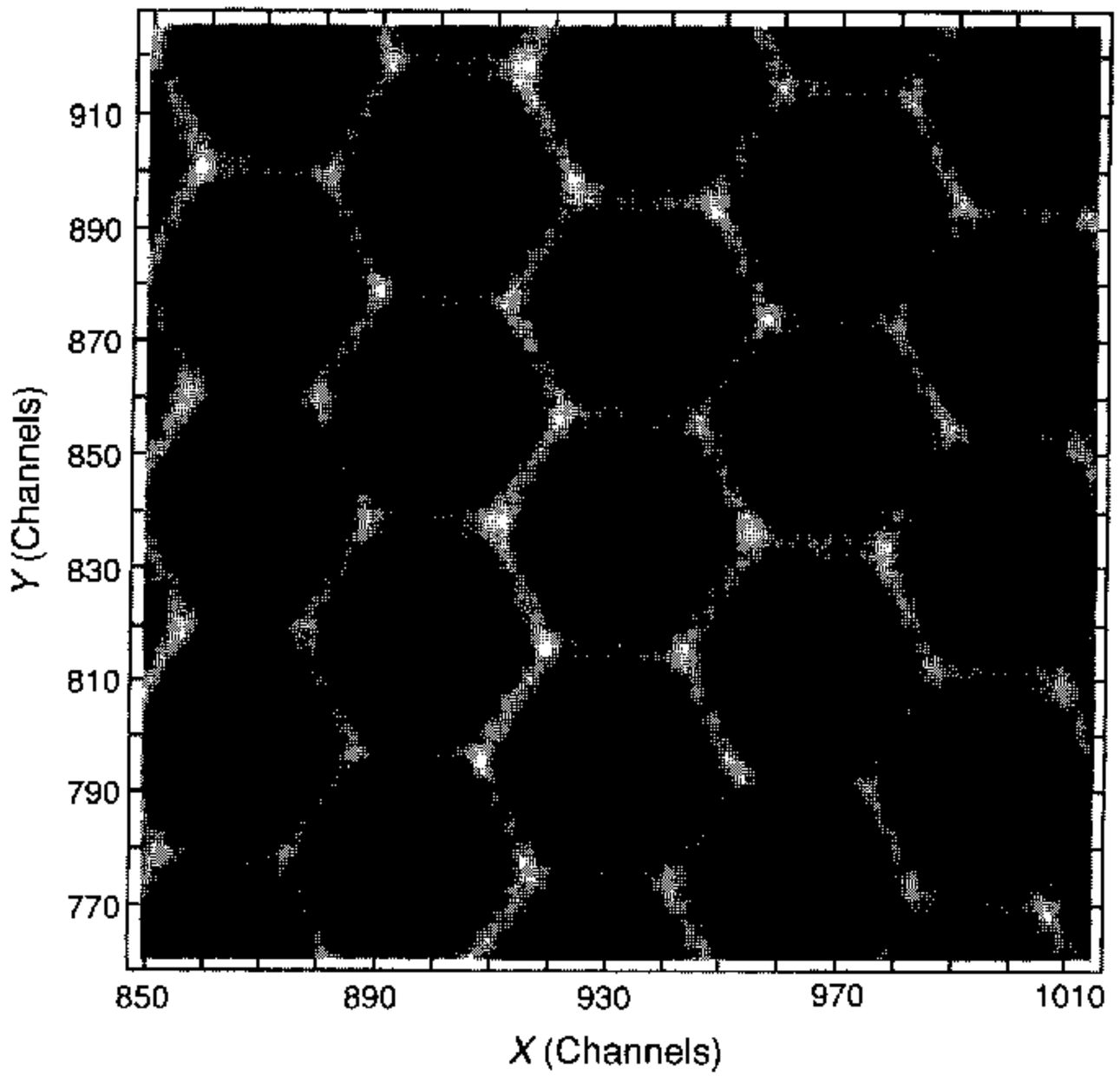

Fig. 6.5. Detail of an image acquired with the DLD [19]. The lines of the mesh were 0.1 mm in diameter. X and Y are given in channel numbers (40 channels = 4 mm).

However, it is not very useful for obtaining the remaining space coordinate via timing information due to the relatively slow electronic read-out of the optical image, and because after each laser shot a complete optical image, which must contain just one event, has to be analysed. A more promising way of using a phosphorescent detector with two cameras was described in the previous chapter by Zajfman, Hebert and Strasser, where fluorescence lifetime measurements of the phosphor screen were used to extract information of the arrival time of each particle. However, in this time-resolved camera the phosphor needs to be selected in accordance with the arrival time distribution of the particles of the process under study. The construction of a DLD is simpler and less expensive than the special imaging CCD cameras and it can be used without modification for different chemical processes.

6.3 Applications of the delay-line detector

6.3.1 Speed and temperatures of the molecular beam

Although the real advantage of the delay-line detector is its ability to determine 3-D product momentum distributions, our technique also provides an excellent

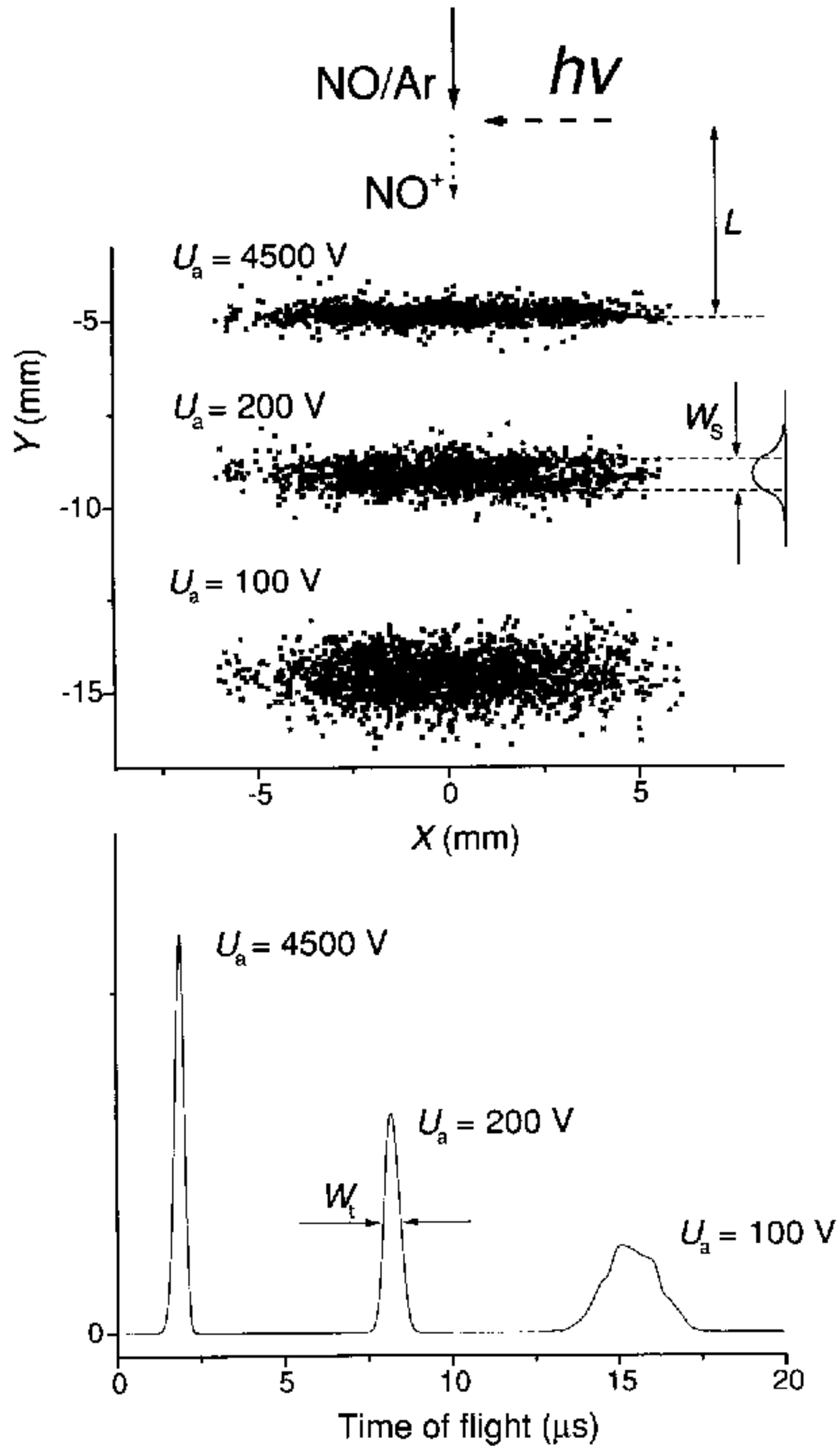

Fig. 6.6. Upper panel: space distribution of NO^+ ions from the 226.2 nm ionization of NO at different acceleration fields. The molecular beam propagates vertically from top to bottom and is intersected by the laser beam at a right angle. The position L of the molecular beam image on the DLD is the product of the average speed of the molecular beam with the time-of-flight. W_s is a measure of the longitudinal speed distribution of the molecular beam. Lower panel: distributions of the times-of-flight for the same three groups of ions. For illustrative purposes the widths W_t of the lines are increased by a factor of 100.

opportunity to study molecular beam properties. Figure 6.6 shows examples of the space distribution of NO^+ ions at different acceleration voltages that are equivalent to different times-of-flight. In these experiments, a diluted (10^{-4}) mixture of NO in $X (X = \text{Ar, He, } N_2)$ was expanded through the nozzle and NO was detected by

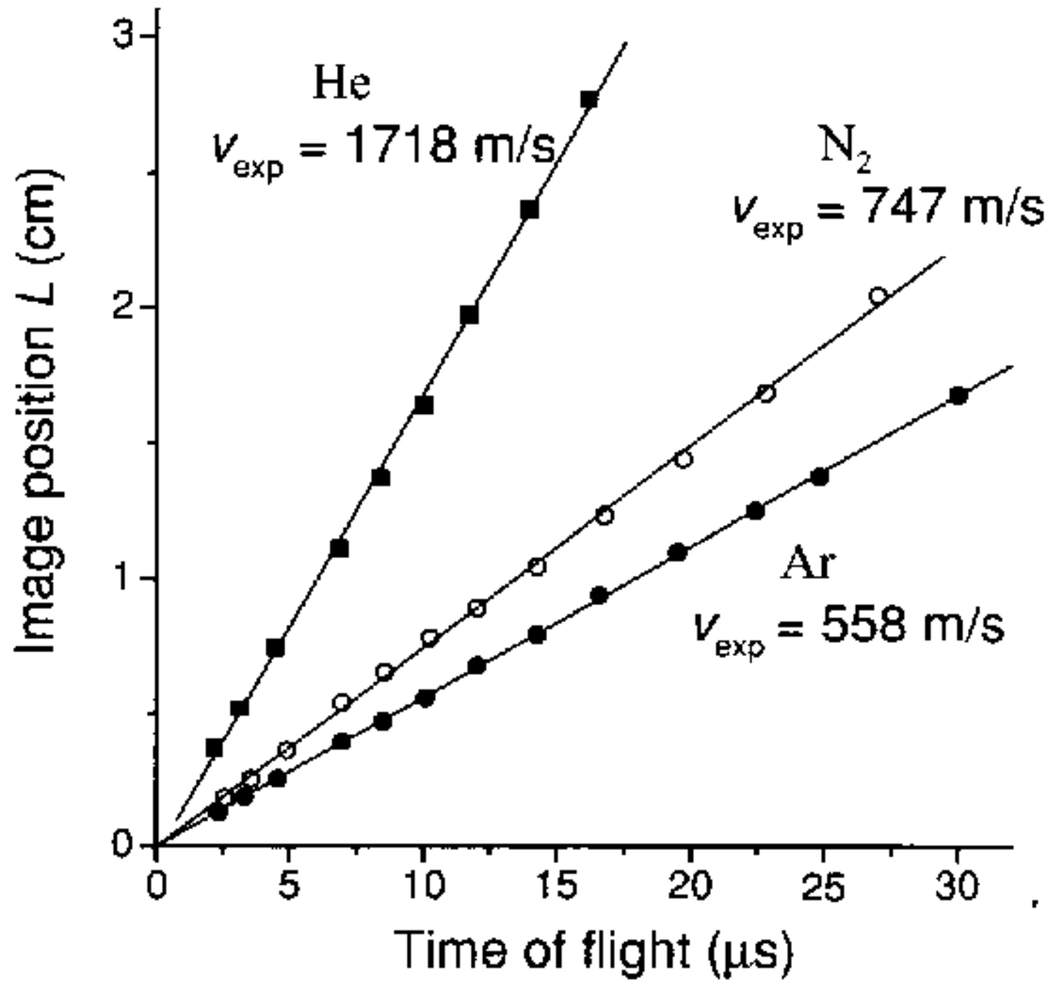

Fig. 6.7. Plot of the position L (Fig. 6.6) versus the time-of-flight t for NO/He, NO/N_2, and NO/Ar yields straight lines the slopes of which are the speeds v_{exp} of the molecular beams.

(1 + 1) REMPI at 226.2 nm. The analysis of the space distributions of NO along the Y axis has shown that the distribution has a Gaussian profile:

$$W(y) = W_0 \exp\left(-\frac{4 \ln 2 (y - L)^2}{W_s^2}\right) \tag{6.1}$$

where y is the space coordinate along the molecular beam axis, L is the position of the image of the molecular beam with respect to the laser beam–molecular beam interaction region, and W_s is the full width at half maximum (FWHM) of the space distribution. The variations of L and W_s with time-of-flight t are shown in Figs. 6.7 and 6.8, respectively, and can be used to calculate the speeds v_{exp} of the molecular beam and the translational temperature T_s.

The method to obtain the speeds v_{exp} of Ar, He, and N_2 molecular beams is quite straightforward: the speeds are the slopes of the linear fits to the data in Fig. 6.7, $v_{exp} = dL/dt$. The maximum theoretical speed of the molecular beam v_{max} may be calculated as

$$v_{max} = \sqrt{\frac{\gamma}{\gamma - 1} \frac{2kT_0}{m}} \tag{6.2}$$

where m is the mass of the buffer gas molecule (He, Ar, N_2, or H_2 in our case), k is the Boltzmann constant, $T_0 = 295$ K is our room temperature, and γ is the ratio of heat capacities, C_P/C_V. The γ parameter is 5/3 and 7/5 for an atomic and

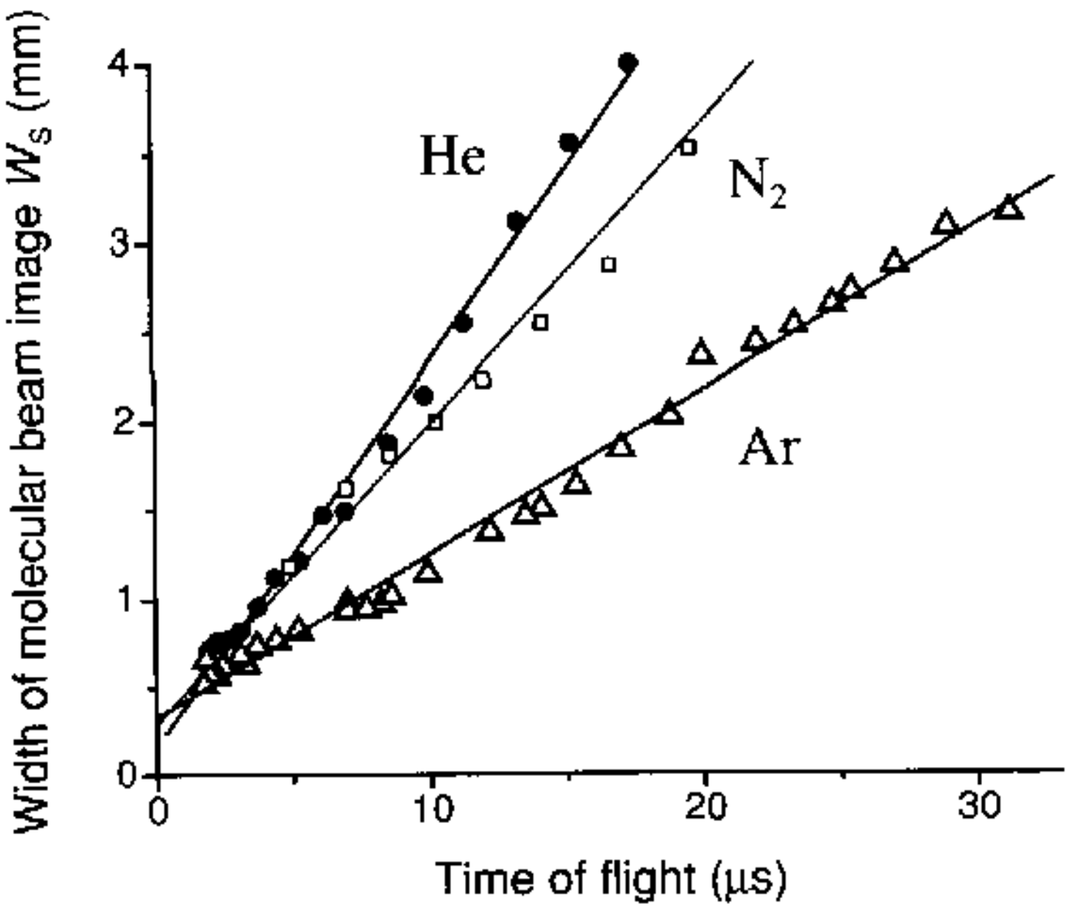

Fig. 6.8. Plot of the longitudinal width W_s of the image of the molecular beam (Fig. 6.6) versus the time-of-flight t for NO/He, NO/N_2, and NO/Ar. The data exhibit the expected linear dependence the slopes of which give the temperatures of the molecular beams, see equation (6.5).

a diatomic buffer gas, respectively. Equation (6.2) assumes that all rotational and translational energies of the molecule are transformed to directed, collective kinetic energy of the beam: the colder the beam, the closer v_{max} and v_{exp} values. Note that the internal temperature of the beam T_{calc} may be obtained from the difference between these speeds:

$$T_{calc} = T_0 \left[1 - \left(\frac{v_{exp}}{v_{max}} \right)^2 \right]. \tag{6.3}$$

The experimentally observed v_{exp} and the calculated v_{max} values are listed in Table 6.1.

Figure 6.8 is an experimental plot of the width W_s as a function of the time-of-flight t. The Gaussian profile of the space distribution is due to the one-dimensional Gaussian speed distribution over the Y axis, which is characterized by the temperature T_s:

$$W(v_y) = W_y \exp\left(-\frac{M(v_y - v_{exp})^2}{2kT_s} \right) \tag{6.4}$$

where M is the mass of the NO molecule. Substituting $v_y - v_{exp} = (y - L)/t$ one can find the relation between W_s and T_s by comparing equation (6.4) with (6.1):

$$T_s = \frac{M\left(\frac{dW_s}{dt}\right)^2}{8k(\ln 2)^2} \tag{6.5}$$

Table 6.1. *Summary of temperatures and speeds of the molecular beams for different buffer gases. v_{max} is the maximum beam velocity which has been calculated assuming complete cooling to a temperature of 0 K, calculated with (6.2); v_{exp} is the experimentally observed value; T_s is the translational temperature of the molecular beam derived from the spread in the v_y velocity component (in beam direction), extracted from the broadening of the impact position on the DLD, see (6.5); T_{rot} is the rotational temperature of the NO molecule extracted from spectroscopic measurements of the intensities of rotational transitions; T_{calc} is the internal temperature of the beam obtained from the difference between v_{exp} and v_{max}, (6.3). The negative calculated temperature for the Ar beam is a consequence of taking the difference of two large quantities with small experimental uncertainties*

Gas	v_{max} (m/s)	v_{exp} (m/s)	T_s (K)	T_{rot} (K)	T_{calc} (K)
Ar	554	558 ± 4	3.5 ± 0.5	3.0 ± 0.5	-4 ± 5
He	1751	1718 ± 12	12.3 ± 2	8 ± 2	11 ± 5
N_2	783	747 ± 12	12.7 ± 2	12 ± 2	26 ± 9
H_2	2931	2041 ± 40			152 ± 6

where dW_s/dt is the slope of the linear fit to the data in Fig. 6.8. The experimental results on T_s are summarized in Table 6.1. Note that the variations of W_t with TOF t can be used to calculate the translational temperature of the beam along the Z axis, where W_t is the width of the TOF distribution (Fig. 6.6). This temperature was found to be very small (about 0.2 K for NO/Ar). Thus, using this simple analysing technique, we can gain information on the beam temperature parallel and perpendicular to the propagation direction of the beam.

6.3.2 Spectroscopy of cold molecules

Another interesting application of the DLD is the REMPI spectroscopy of cold molecules. It is well known that in ultra-cold supersonic beams a considerable simplification of molecular spectra can be achieved. Here, one problem is the contribution of room-temperature background molecules and impurities which make the spectra more difficult to analyse. In time-of-flight experiments with a perpendicular geometry of molecular beam and spectrometer axis it is easy to distinguish between contributions from the molecular beam and background contributions since the particles which belong to the molecular beam are located on a very small area of the DLD which is shifted from the axis of the laser by the distance $L = v_{exp}t$. Here t is the TOF and v_{exp} is the experimentally determined speed of the molecular beam (Fig. 6.9).

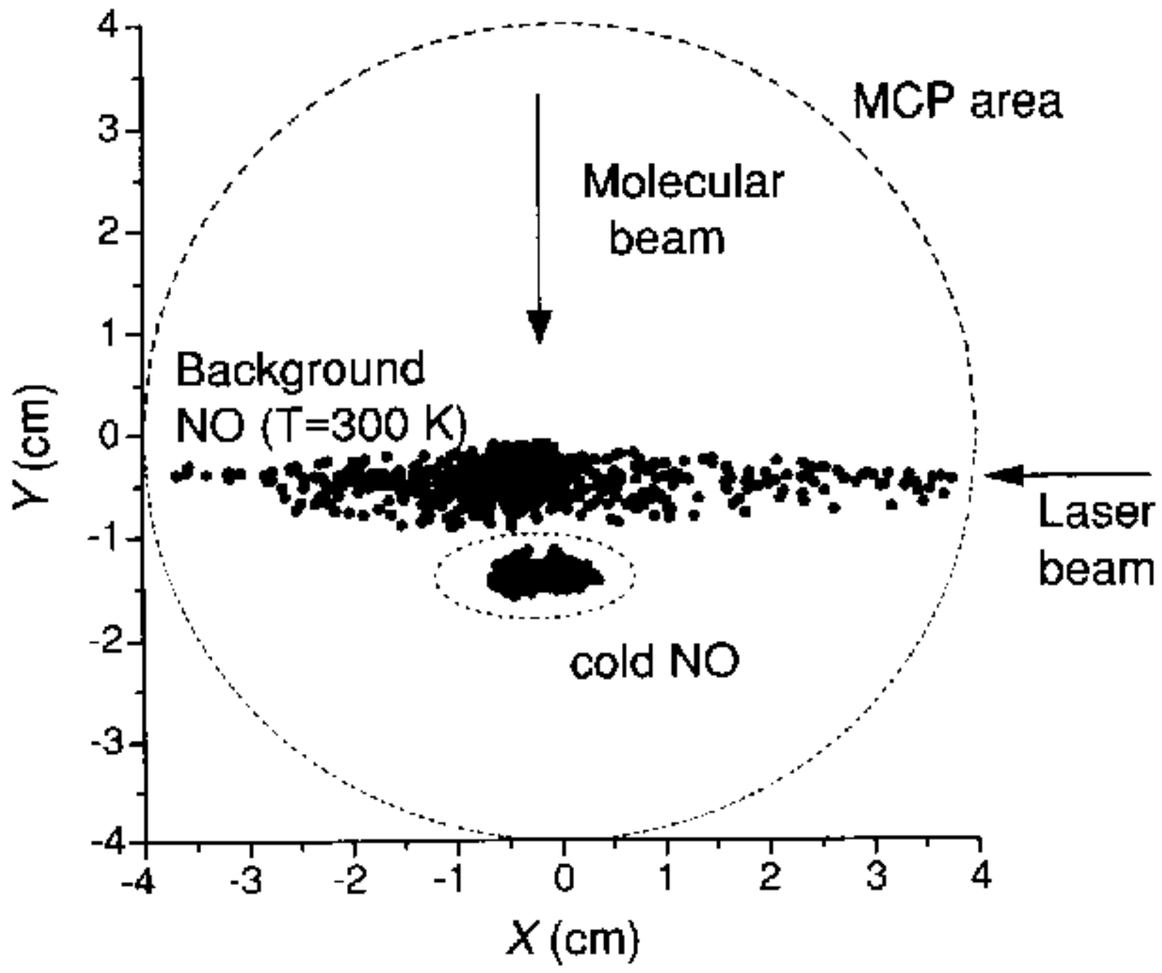

Fig. 6.9. Space distribution of NO^+ ions from the 226.2 nm ionization of NO. Ions from the molecular beam are located in a small area marked by the dotted ellipse. Only these ions are used to construct the rotational REMPI spectrum of NO.

This method allows, for example, the determination of the rotational temperature T_{rot} of NO in Ar, He, and N_2 molecular beams (Fig. 6.10). In general, there exists a good agreement between the temperatures T_{rot}, T_{exp}, and T_s as summarized in Table 6.1.

6.4 Classic photofragment imaging: photolysis of Cl_2

6.4.1 Experimental results

The quality of the 3-D imaging technique was examined by studying the well-known photolysis of molecular chlorine, $Cl_2 + h\nu$ (355 nm) $\rightarrow$ 2 Cl($3p\ ^2P_{3/2}$).

In the experiments the third harmonic of a Nd:YAG laser (355 nm) was used to photolyse Cl_2, and a Nd:YAG laser pumped dye laser was used for the (2 + 1) REMPI detection of ground state Cl($^2P_{3/2}$) atoms at 235.336 nm. In such measurements the wavelength of the probe laser radiation was scanned over the Doppler broadened absorption line in order to realize an unbiased detection of all Cl atoms regardless of the v_x component of their velocity. An example of 3-D speed distributions of Cl atoms obtained in this way is shown in Fig. 6.11. Each data point contains information on the velocity components v_x, v_y, v_z. However, due to the restrictions of a 2-D black and white picture, only a projection of this real 3-D distribution can be seen.

The 3-D image of Fig. 6.11 consists of two overlapping spherical distributions: the first (lower) one corresponds to fragments from cold Cl_2 in the molecular beam, and the second (upper) one corresponds to fragments from background Cl_2

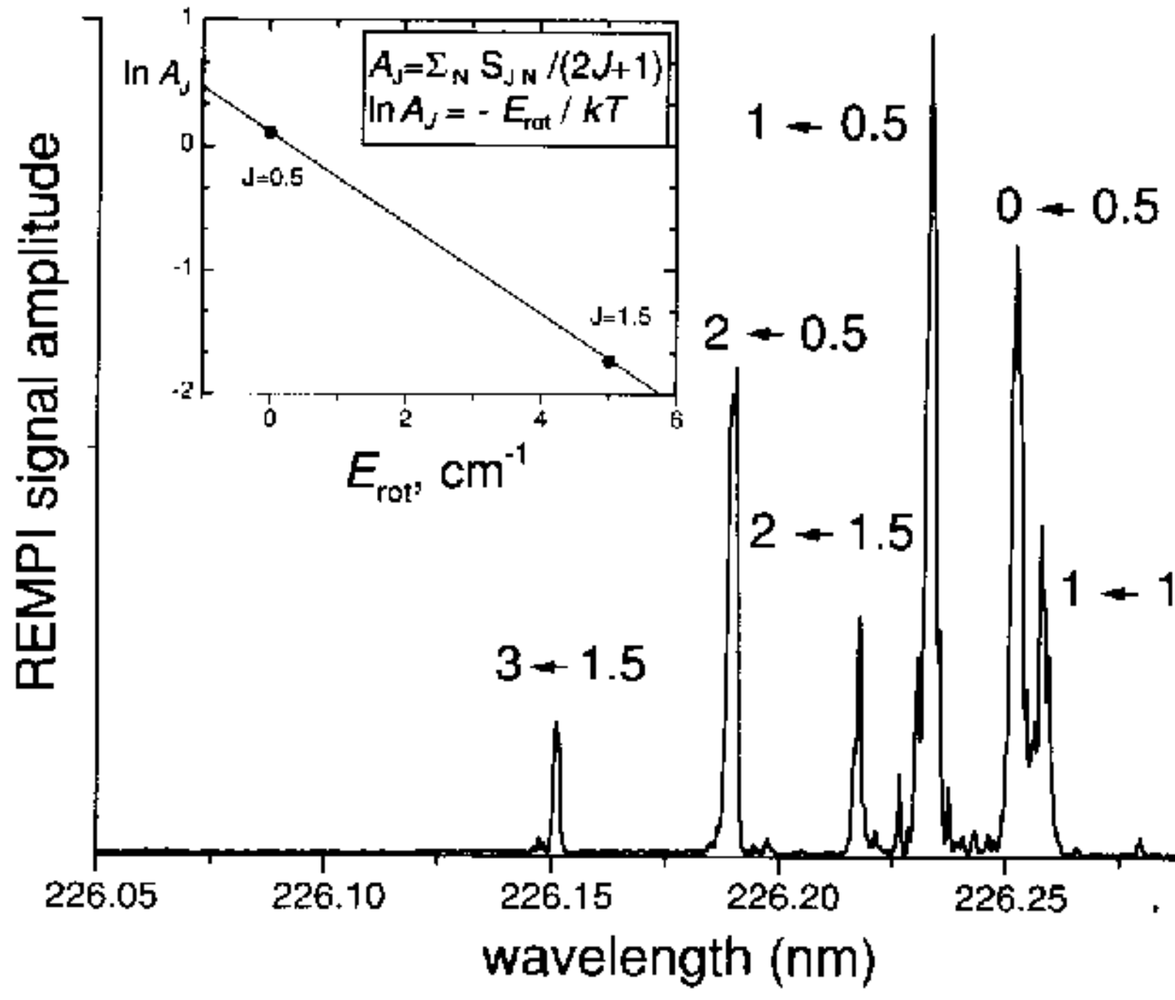

Fig. 6.10. Rotational REMPI spectrum of NO in the cold Ar molecular beam. Only ions from a small area marked by the dotted ellipse in Fig. 6.9 are taken into account. The assignment of the rotational transitions is indicated. In the upper left corner: simplified determination of the rotational temperature T_{rot} of NO. S_{JN} is the peak area for a single $N \leftarrow J$ transition, A_J is the cumulated peak area for all transitions originating from a single J level after correcting for degeneracy.

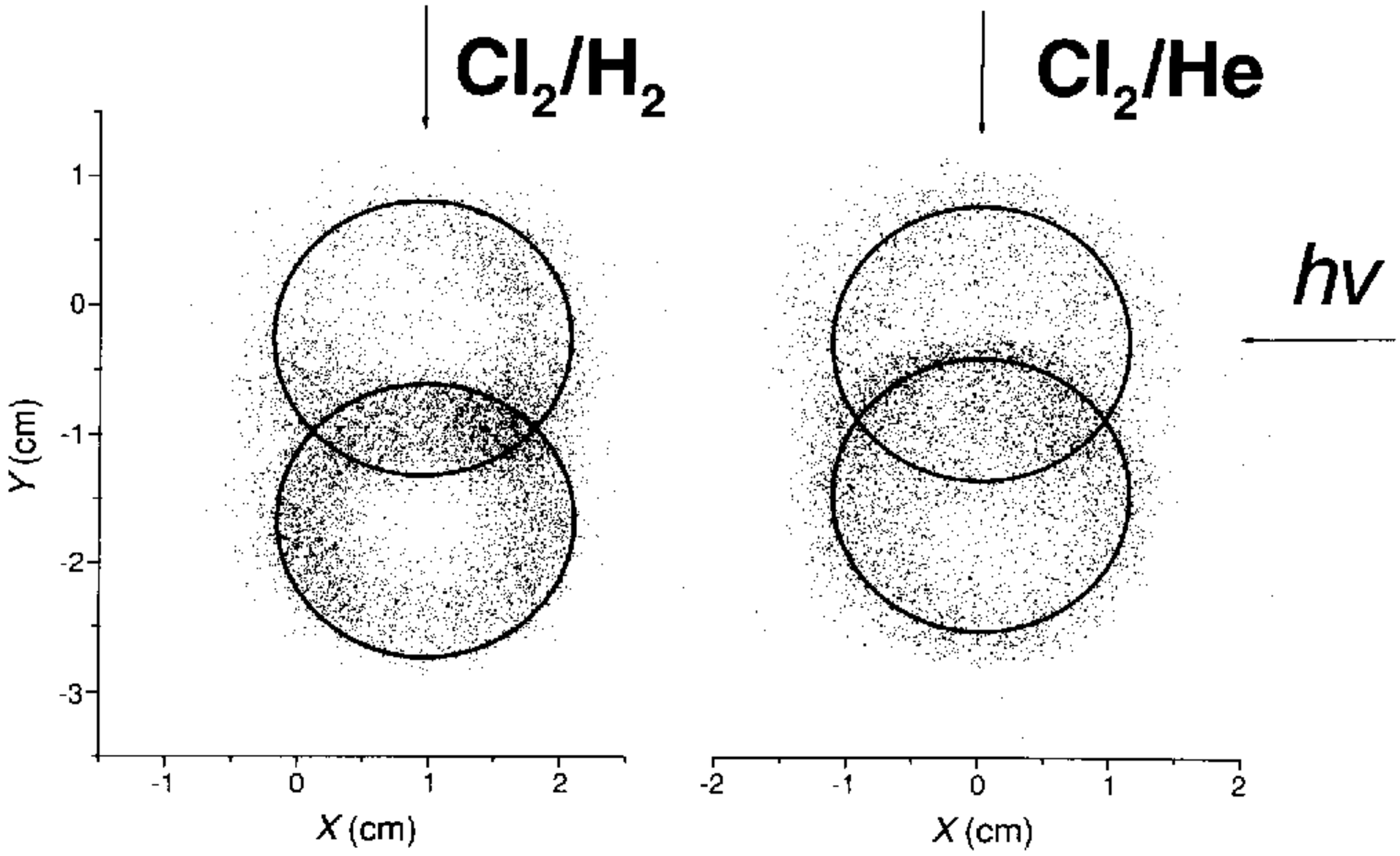

Fig. 6.11. The 2-D representation of the full 3-D speed distributions of Cl atoms generated in the photolysis of Cl_2 in Cl_2/H_2 and Cl_2/He molecular beams. The lower spheres result from Cl fragments from the photolysis of cold Cl_2 in the molecular beam, whereas the upper spheres result from Cl fragments from thermal background Cl_2. Circles indicate the centres of the Cl fragment speed distributions shown in Fig. 6.13.

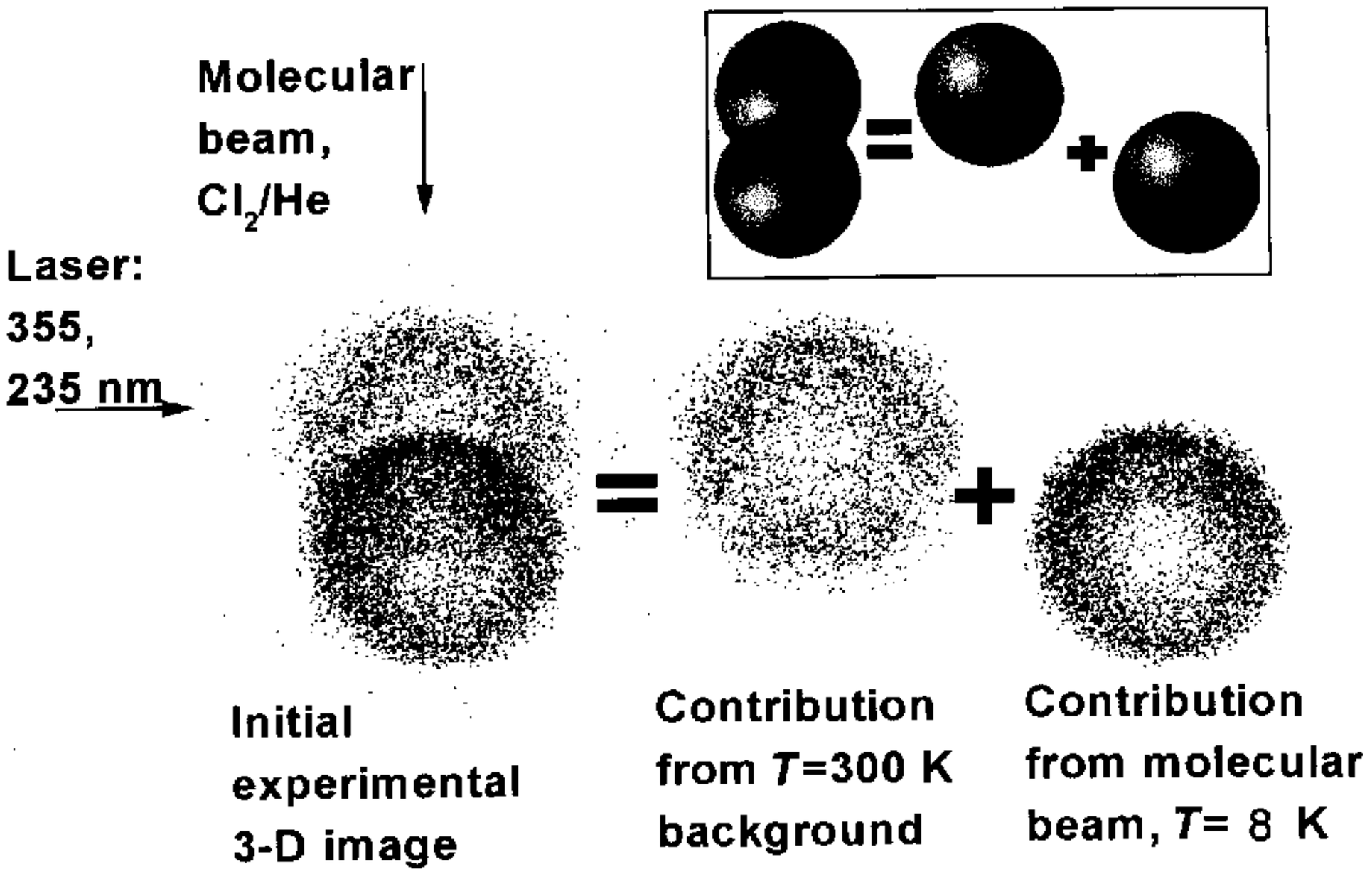

Fig. 6.12. The 3-D images of the Cl atom distribution can easily be divided in two parts which is not possible with conventional 2-D images. In the upper corner this separation procedure is shown schematically: the experimental 3-D spherical distributions are replaced by half-translucent spheres.

at room temperature. Again, the centres of both distributions are shifted by the distance $L = v_{exp}t$. Thus, from Fig. 6.11 one may easily determine the speed of the molecular beam from the distance between the two rings divided by the TOF. The H_2 beam has been found to be slightly faster than the He beam, see Table 6.1. Now one can, for example, separate these distributions, as is schematically shown in Fig. 6.12, and exclusively study the speed distribution from the dissociation of cold molecules free from background interference. This separation is easily feasible, since for every single event depicted in Fig. 6.11, the knowledge of all three components of the velocity unequivocally determines to which sphere the fragment belongs. This situation is completely different from a conventional 2-D image, because in a 2-D image the spheres occur as two circles and within the common area of these two circles it is impossible to know which data point belongs to which distribution.

The result of our 3-D Cl_2 study is shown in Fig. 6.13. In principle, the Cl fragment speed distribution, hence also the distribution of its kinetic energy E_{kin}, should be single-valued: $E_{kin}(Cl) = \frac{1}{2}[h\nu - D_0(Cl)]$, where the (small) internal energy of the parent molecule has been neglected. Here, $h\nu$ is the energy of the dissociating photon, and D_0 is the dissociation energy for the atomization of the chlorine

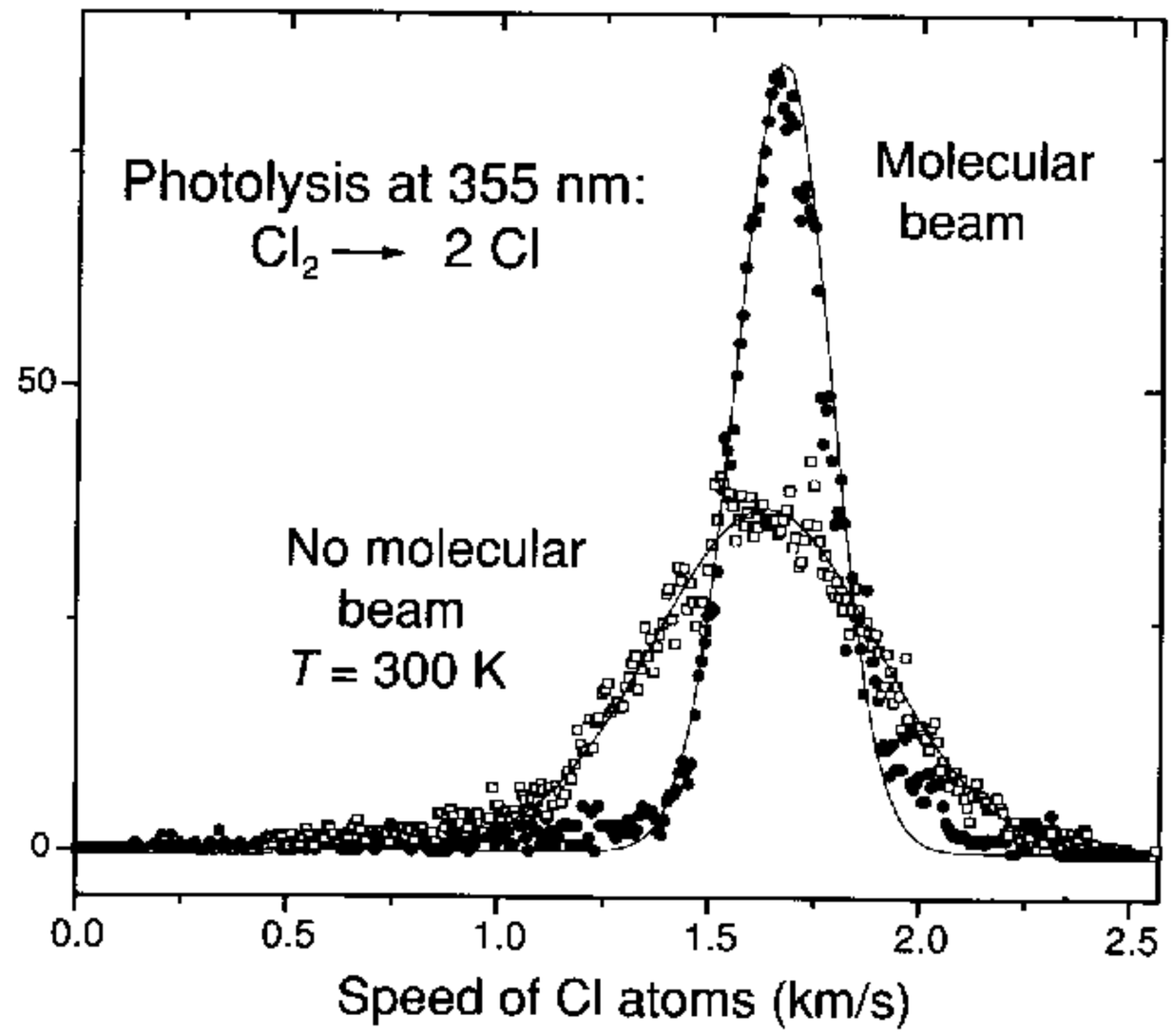

Fig. 6.13. Speed distributions of Cl fragments from the photodissociation of Cl_2 obtained from 3-D images (see Figs. 6.11, 6.12) for a Cl_2/He molecular beam.

molecule. However, this very small thermal energy after cooling of the parent in the supersonic expansion in conjunction with the response function of the apparatus leads to a small broadening of the speed distribution as depicted in Fig. 6.13. We determined not only the average width of the speed distribution of Cl, but also the widths along all three axes. It was found that these widths are different and exhibit a different dependence on the acceleration voltage. The main anisotropic factors, which contribute to the width of the distribution, are the length of the laser spot, rotation of Cl_2, and the speed dispersion of Cl_2 in the molecular beam. From Fig. 6.13 it can be seen that also the widths of the distributions for room-temperature and cold Cl_2 parent molecules are different because of the different speed dispersions and rotational energies.

6.4.2 Spatial fragment anisotropy – how to calculate the β parameter

From the observed 3-D distributions not only the speed distribution can be extracted as demonstrated in the previous section, but it is also possible to determine the angular distribution of the photofragments for any given speed value v. Before specific examples are dealt with, the general approach to studying angular distributions of photodissociation products will be considered. The normalized angular distribution of photofragments with a single given speed with respect to the polarization vector **E** of the electromagnetic field of the photolysis laser is, as we are now familiar,

written as

$$P(\theta, \varphi) = \frac{1}{4\pi}[1 + \beta P_2(\cos\theta)]. \tag{6.6}$$

Here θ and φ are the polar and the azimuthal angle of the photofragment recoil velocity $\boldsymbol{v}$ with the polarization vector $\mathbf{E}$, β is the anisotropy parameter which characterizes the angular distribution, and $P_2(x)$ is the second-order Legendre polynomial: $P_2(x) = \frac{1}{2}(3x^2 - 1)$. $P(\theta, \varphi)$ is normalized such that

$$\int_0^{\pi} \sin\theta d\theta \int_0^{2\pi} d\varphi\, P(\theta, \varphi) = 1.$$

If the integration over φ is performed, then a distribution $P_{\text{th}}(\theta)$ with respect to the polar angle may be defined:

$$P_{\text{th}}(\theta) = \tfrac{1}{2}\, \sin\theta[1 + \beta P_2(\cos\theta)] \tag{6.7}$$

such that

$$\int_0^{\pi} P_{\text{th}}(\theta)d\theta = 1.$$

The β parameter ranges from -1 to $+2$ with an isotropic distribution of the fragments corresponding to $\beta = 0$. Most often, the β parameter is considered to be independent of the fragment velocity. However, this need not be the case. Especially, the broader the kinetic energy distribution becomes, the more important becomes the velocity dependence of β, and the more information on the dynamics of a reaction is contained in this velocity dependence. An interesting application of the 3-D technique is the study of this dependence. This means that we must calculate the β parameter for a group of photofragments that have a velocity within the range $v_0 < v < v_1$. The experimental distribution of the photofragments over the angle θ is given by the function $P_{\text{exp}}(\theta)$. The β parameter may be determined from the condition

$$\frac{\partial}{\partial\beta} \int_0^{\pi} [P_{\text{exp}}(\theta) - P_{\text{th}}(\theta)]^2 d\theta = 0. \tag{6.8}$$

The normalized experimental distribution of the photofragments over the angle θ may be calculated as

$$P_{\text{exp}}(\theta) = \frac{1}{N} \sum_{i=1}^{N} \delta(\theta - \theta_i), \tag{6.9}$$

where $\delta(x)$ is a delta-function, θ_i is the polar angle for the i-th photofragment, and the summation is performed over particles with velocities in the range of consideration. N is the number of these particles. Inserting (6.9) into (6.8) gives the final result

$$\beta = {}^4\!/_5\,(32B_1/\pi + 1) \tag{6.10}$$

where $B_j = \frac{1}{N}\sum_i \sin\theta_i[P_2(\cos\theta_i)]^j$.

The β parameter can also be obtained from a subset of the observed photofragments if the range of the angle θ is accordingly constrained. For example, in the **E** || **Z** case a contribution from ^{37}Cl atoms to the distribution of ^{35}Cl atoms occurs at some range of the angle θ. Usually, we want to get rid of this contribution. Let us determine the β parameter for a group of the photofragments that are situated in the range $a \le \theta \le b$. The same approach gives the final result

$$\beta = -\frac{A_0^2 B_1 - A_0(A_1 B_0 + C_1) + A_1 C_0}{A_0(A_1 B_1 - C_2) - A_1(A_1 B_0 - C_1)} \tag{6.11}$$

where $A_j = \int_a^b [P_2(\cos\theta)]^j \sin\theta\, d\theta$ and $C_j = \int_a^b [P_2(\cos\theta)]^j \sin^2\theta\, d\theta$. Applying (6.10) or (6.11) to experimental results one can find the $\beta(v)$ dependence.

Concerning the photolysis of Cl_2, at 355 nm the perpendicular optical transition $^1\Pi_{1u} \leftarrow {}^1\Sigma_{0_g^+}$ contributes to more than 90% of the light absorption [22–24]. The excited state is repulsive, so the dissociation is fast and the β parameter must be close to its limiting value of -1. The value determined from our experimental data is $\beta = -1.00 \pm 0.05$ and agrees excellently with previous measurements and theoretical calculations [22].

6.5 Beyond the classic application: modern developments

6.5.1 Atomic photofragment alignment

The strength of the 3-D imaging method lies in the straightforward investigation and analysis of processes where the cylindrical symmetry of the fragment distribution is broken. One such example is the photofragment angular momentum polarization (orientation and alignment) in a photodissociation process. Fragments produced by (circularly or linearly) polarized photolysis may be oriented and/or aligned, that means that they exhibit nonequilibrium populations of the m_J and $|m_J|$ magnetic sublevels, respectively. Measurements of the angular momentum polarization as a function of the recoil velocity vector (**v**–**J** correlation) provide the most detailed information on the dissociation dynamics. While this property has been studied for rotating diatomic photofragments for over a decade, the atomic **v**–**J** correlation has been observed only recently [25–29]. Note that in most essential

details, there is little similarity between atomic and molecular photofragment phenomena.

We consider only the case of monoenergetic atomic photofragments produced by linearly or circularly polarized photolysis radiation, and detected by a linearly or circularly polarized probe laser via (2 + 1) REMPI. In the case of linearly polarized photolysis and probe laser radiation, polarization geometries may be realized where the polarization directions are oriented parallel or perpendicular to each other. The angular distribution of the atoms is then given by [28]

$$I_{||}(\theta, \varphi) = \left[1 + \frac{\beta}{2}(3x - 1)\right] + V(a_1 + a_2 x + a_3 x^2) \tag{6.12}$$

$$I_{\perp}(\theta, \varphi) = \left[1 + \frac{\beta}{2}(3x - 1)\right] - \frac{V}{2}(a_1 + a_2 x + a_3 x^2) - \frac{3V}{4}(1 - x)\left(a_4 + \frac{2}{3}a_1 x\right)\cos 2\varphi \tag{6.13}$$

where $V = \frac{5R_2}{R_0}\sqrt{\frac{J(J+1)}{(2J+3)(2J-1)}}$ and $x = \cos^2\theta$. θ and φ are the spherical angles with respect to the dissociation laser polarization, the direction of the dissociation laser beam is $\theta = 90°$, $\varphi = 0°$. The β and the a_i are parameters that may be extracted from experiment by fitting the distributions from (6.12) and (6.13) to the experimentally observed data. The a_i parameters are connected to dynamical parameters characterizing the dissociation process by (6.14). J is the electronic angular momentum of the initial state of atoms, which is assumed to be small ($J < 2$). Otherwise the expressions for the distributions are more complex. The alignment sensitivity parameter R_2/R_0 depends on the transition involved to detect the atoms. For example, for (2 + 1) REMPI detection of the ground state $Cl(^2P_{3/2})$ atoms via the intermediate $^2S_{1/2}$ and $^2D_{5/2}$ states (236.284 and 234.640 nm, respectively) the parameter is equal to -1 and 5/7, respectively [28].

Using the expressions

$$\begin{pmatrix} a_1 \\ \frac{1}{3}a_2 \\ \frac{1}{3}a_3 \\ a_4 \end{pmatrix} = \begin{pmatrix} -1 & -1 & 0 & -3 \\ 1 & 2 & -1 & 2 \\ 0 & -3 & 1 & -1 \\ 1 & 1 & 0 & -1 \end{pmatrix} \begin{pmatrix} \frac{1}{2}s_2 \\ \frac{1}{2}\alpha_2 \\ \gamma_2 \\ \frac{1}{4}\eta_2 \end{pmatrix} \tag{6.14}$$

one can obtain the s_2, α_2, γ_2, and η_2 alignment anisotropy parameters, which are responsible for different excitation mechanisms of the parent molecule.

Consider briefly, for example, the photolysis of Cl_2 at 355 nm [28]. The excited states $C^1\Pi_{1u}$ and $A^3\Pi_{1u}$ can be optically excited from the ground state $X^1\Sigma_{0_g^+}$ of the molecule, the contribution to the light absorption is $> 90\%$ and $< 10\%$, respectively. The photodissociation via $A^3\Pi_{1u}$ state does not produce alignment

of Cl atoms, consequently the alignment occurs only via the $C^1\Pi_{1u}$ state. For the photodissociation of Cl_2 by linearly polarized radiation near 355 nm theory predicts the relations

$$\alpha_2 = {}^1\!/_2 s_2 = -{}^2\!/_{25}(1-w), \quad \eta_2 = -{}^4\sqrt{6}/_{25} w_{\mathrm{coh}}, \quad \gamma_2 = 0, \tag{6.15}$$

where w is the probability of a nonadiabatic transition from $C^1\Pi_{1u}$ to $A^3\Pi_{1u}$ and w_{coh} is the 'coherent' off-diagonal nonadiabatic transition matrix element. In other words, $w = |< C|V|A >|^2$ and $w_{\mathrm{coh}} = \mathrm{Re}[< C|V|A >< C|V|C >^*]^2$. Here V is the operator responsible for the non-adiabatic transition, $< C|$ and $< A|$ denote excited electronic states, and $\Omega = 1$ is assumed in all cases. The experimental values for the alignment anisotropy parameters may be rather well reproduced by (6.15) with $w = 0.60 \pm 0.04$ and $w_{\mathrm{coh}} = -0.19 \pm 0.05$.

The 3-D imaging technique is the most appropriate method for this kind of investigation, since the angular distributions $I_{||}(\theta, \varphi)$ and $I_{\perp}(\theta, \varphi)$ are measured directly. Otherwise the 3-D distributions must be reconstructed from the 2-D images, as was done in the above-mentioned study of photodissociation of Cl_2.

6.5.2 Application of 3-D detection to photodissociation processes

In the study of photodissociation dynamics the experimental goal is simple in concept: to detect and characterize the products resulting from photon absorption, and to determine the effect of photon energy and polarization on the nature and distribution of these products. Until recently the angular distribution of the products was generally characterized by a single, velocity-independent β parameter (6.6). Now the combination of molecular beam techniques with REMPI/TOF mass spectrometry allows us to obtain more detailed information, for example, the dependence of the β parameter on the particle velocity v.

6.5.3 Angular distribution of photofragments: 'core-sampling' technique

In principle, the determination of the $\beta(v)$ dependence does not require 3-D or 2-D imaging techniques. Let us briefly consider an experiment performed by K. Liu and co-workers [30] in which the photodissociation of NO_2 at 355 nm was studied:

$$NO_2 + h\nu \rightarrow NO(^2\Pi_\Omega) + O(^3P_J).$$

Oxygen atoms in all three spin-orbit states $O(^3P_J)$ (J = 2, 1, 0) were state-selectively ionized by a (2 + 1) REMPI detection scheme around 226 nm [31]. The TOF spectra of the $O(^3P_J)$ atoms were monitored by the 'core-sampling' technique which detects only the 'core distribution', i.e., those ions with very small v_x and v_y components. The selection of the ions with $v_x \approx v_y \approx 0$ was achieved by placing a small aperture

in front of the ion detector. Generally, the photofragment centre of mass velocity distribution over speed v and angle θ can be expressed as

$$P(v, \theta) = g(v)[1 + \beta(v)P_2(\cos\theta)], \tag{6.16}$$

where the speed distribution $g(v)$ and $\beta(v)$ are unknown functions. Normalization factors are included in the $g(v)$ dependence. Then the TOF spectra for both polarization directions of the photolysis radiation may be expressed as

$$\begin{array}{lll} \theta = 0^\circ & \mathbf{E} \parallel \mathbf{Z} & P_{\parallel}(v) = g(v)[1 + \beta(v)] \\ \theta = 90^\circ & \mathbf{E} \perp \mathbf{Z} & P_{\perp}(v) = g(v)[1 - {}^1/_2\beta(v)] \end{array}$$

where **E** is the electric field vector of the photolysis radiation. After normalization, the functions $P_{\parallel}$ and $P_{\perp}$ may be used to obtain $\beta(v)$:

$$\beta(v) = 2\frac{P_{\parallel}(v) - P_{\perp}(v)}{P_{\parallel}(v) + 2P_{\perp}(v)}. \tag{6.17}$$

This expression was applied to the experimental data and $\beta(v)$ was determined for all three states of $O(^3P_J)$ (Fig. 6.14). The β distributions for all three sublevels of the $O(^3P_J)$ state display a downward trend with the increase in rotational, vibrational, and spin-orbit energy of NO. The explanation of this trend seems to be quite straightforward: if the photon energy is redistributed over vibrations of NO_2, then the $O(^3P_J)$ atoms are distributed over a wider range of angles. Consequently, β becomes smaller, the rotational and vibrational excitation of NO become higher and the kinetic energies of NO and $O(^3P_J)$ become smaller.

It should be noted, however, that whereas 3-D imaging by a DLD is universally applicable regardless of the specific form of the spatial fragment distribution, core sampling is in exactly the same way limited to the investigation of cylindrically symmetric fragment distributions as photofragment imaging and velocity mapping. Basically, the simultaneous measurement of two dimensions by a PSD is substituted by a sequence of two one-dimensional measurements with identical information content.

6.5.4 Application of 3-D detection to the photolysis of $COCl_2$

The 3-D photofragment imaging technique is a much more powerful and general method than the core-sampling technique discussed above. First, the 3-D imaging technique deals with much more detailed information because the complete 3-D velocity distribution is obtained directly. Second, background contributions from room-temperature molecules or from other ions with the same mass-to-charge ratio may easily be removed. Finally, 3-D imaging does not deal with the profile of

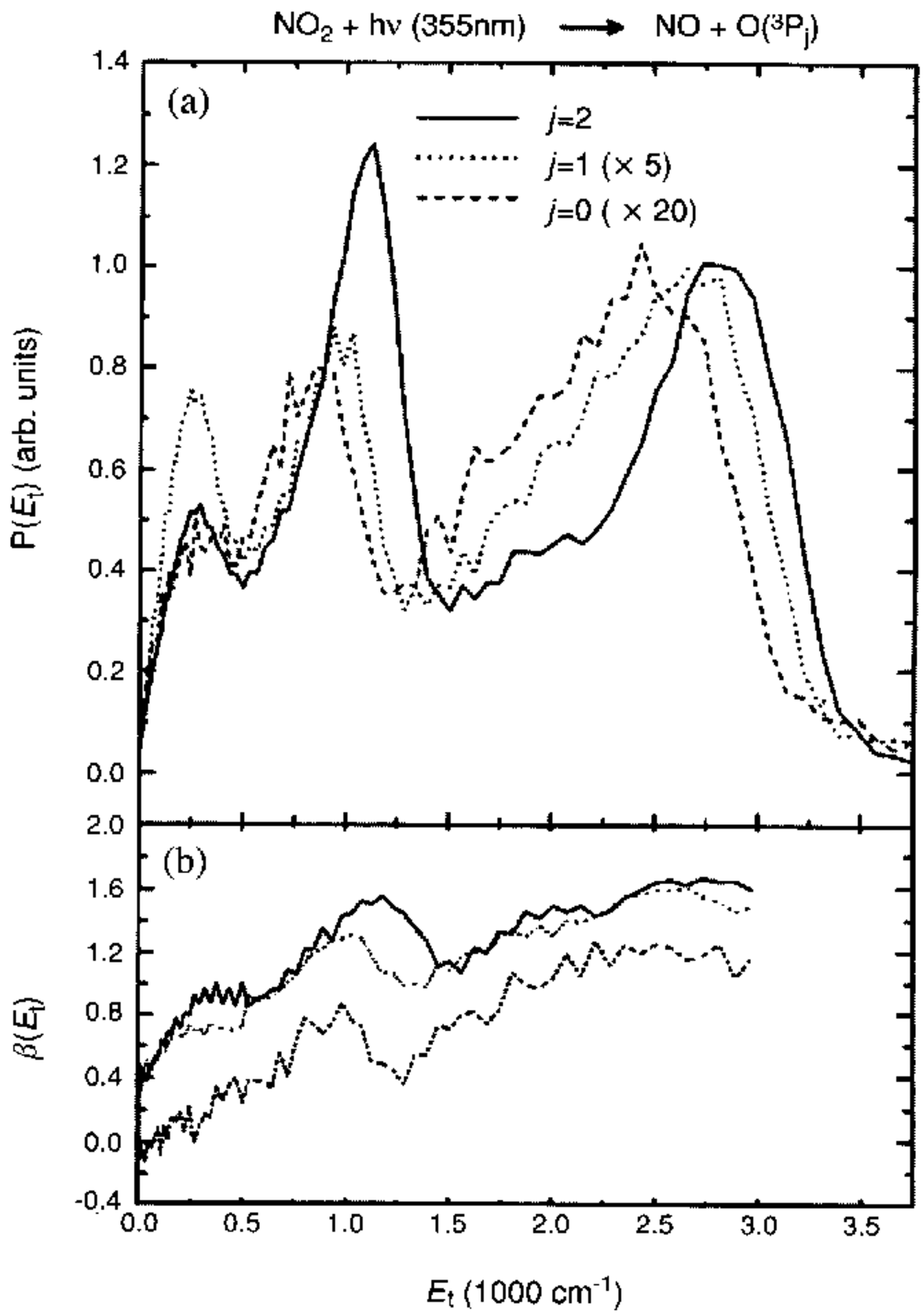

Fig. 6.14. (a) Photofragment centre of mass translational energy distributions from the photodissociation of NO_2 at 355 nm [30]. The results, normalized by the relative populations 1:0.21:0.05, for the $J = 2$, 1, and 0 fine-structure states of $O(^3P_J)$ are represented by solid, dotted, and dashed lines, respectively. (b) The dependence of the β parameters on the Cl fragment translational energy for the three states of $O(^3P_J)$.

an analogue signal which may be sensitive to the apparatus broadening function, saturation of the MCP assembly etc.

A very promising subject for the application of 3-D photofragment imaging techniques is the photoinduced three-body decay

$$ABC \rightarrow A + B + C,$$

where A, B and C may be atoms, diatomics or polyatomics. The three-body processes are important since they govern complex chemical reactions including combustion processes and atmospheric chemistry, and they are much more complicated

in comparison with common two-body decays. The first question aims at the mechanism of a three-body decay, which may be sequential, synchronously concerted, or asynchronously concerted. We call the three-body decay sequential if the time between the first step, ABC $\rightarrow$ AB + C, and the second step, AB $\rightarrow$ A + B, is greater than the mean rotational period of the AB fragment. Otherwise, the decay is considered to be concerted. A synchronously concerted mechanism assumes the linear momenta of A and C fragments to be equal, whereas an asynchronously concerted mechanism does not. A very illustrative, yet oversimplifying picture of synchronously and asynchronously concerted mechanisms is decays via symmetric and antisymmetric stretching modes of a linear ABA parent molecule, respectively. The mechanism of the decay can be understood entirely by examining the spatially and temporally resolved photodissociation products.

A very good example suited to illustrate the subject is the photodissociation of phosgene:

$$COCl_2 + h\nu \rightarrow CO + 2Cl \qquad D_0(\text{Cl–CO–Cl}) = 3.56\,\text{eV}$$

where $E_{av} = h\nu - D_0 = 1.716$ eV is the energy available to the products resulting from 235 nm photolysis. It is well known that in this process two-body decay channels (Cl + COCl, CO + Cl_2) are negligible [32,33]. In our experiments the Cl atoms in both spin-orbit states Cl(^2P_J) (J = 3/2, 1/2) were state-selectively ionized by a (2 + 1) REMPI detection scheme around 235 nm [34]. The 3-D velocity distributions were obtained according to the procedure described in the previous section. The speed distribution and the $\beta(v)$ dependence for ground state Cl($^2P_{3/2}$) are shown in Fig. 6.15. This is a rather simple picture, which can easily be interpreted. From Fig. 6.15 it can be seen that the velocity distribution of Cl atoms consists of two peaks. For one of them the β parameter is close to 0 and for the other one the β parameter is about 0.5.

Evidently, the fast Cl atoms are produced in the first step, $COCl_2 \rightarrow COCl^* + Cl$, because their angular distribution is anisotropic. The slow Cl atoms are produced in the second step, $COCl^* \rightarrow CO + Cl$, which produces an almost isotropic angular distribution of Cl atoms. This means that the decay of $COCl_2$ is asynchronously concerted, or sequential, with a rather large time between the first and the second steps. This description of the decay of $COCl_2$ is too simple, however, since the distributions for the ground state Cl($^2P_{3/2}$) and spin-orbit excited state Cl($^2P_{1/2}$) are different from each other. According to a more detailed analysis, about 80% of the decay correspond to the asynchronously concerted mechanism and about 20% to the synchronously concerted mechanism [32,33].

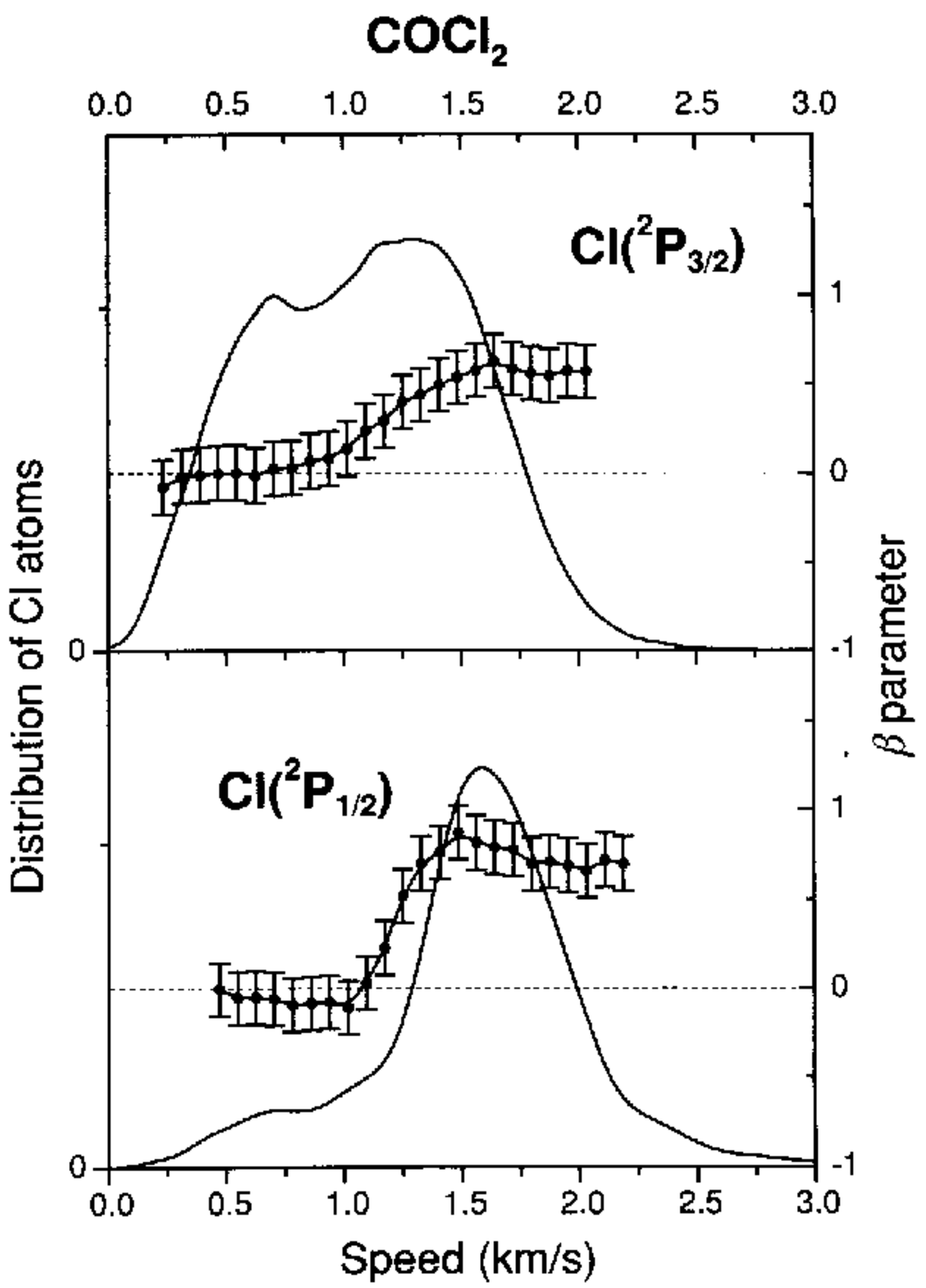

Fig. 6.15. Velocity distributions for the ground state $Cl(^2P_{3/2})$ and excited $Cl(^2P_{1/2})$ atoms in the photolysis of $COCl_2$. The dependence of the β parameters on the Cl fragment velocity (right scale) is shown by curves with error bars.

6.5.5 Photolysis of $SOCl_2$: 3-D detection of Cl atoms

Another example of a three-body decay studied by the 3-D imaging technique is the photodissociation of $SOCl_2$ at 235 nm. At this wavelength there are two energetically possible channels that give Cl atoms:

$$SOCl_2 + h\nu \rightarrow SO + 2\,Cl,\ SOCl + Cl.$$

The speed distribution and $\beta(v)$ dependence for ground state $Cl(^2P_{3/2})$ atoms are similar to those for the dissociation of $COCl_2$ (Fig. 6.16). From Fig. 6.16 it can be seen that the Cl atoms may be separated into two groups, fast and slow. The angular distribution of the fast atoms is rather anisotropic and hence they are produced in the first step, $SOCl_2 \rightarrow SOCl^* + Cl$, while the slow Cl atoms are produced

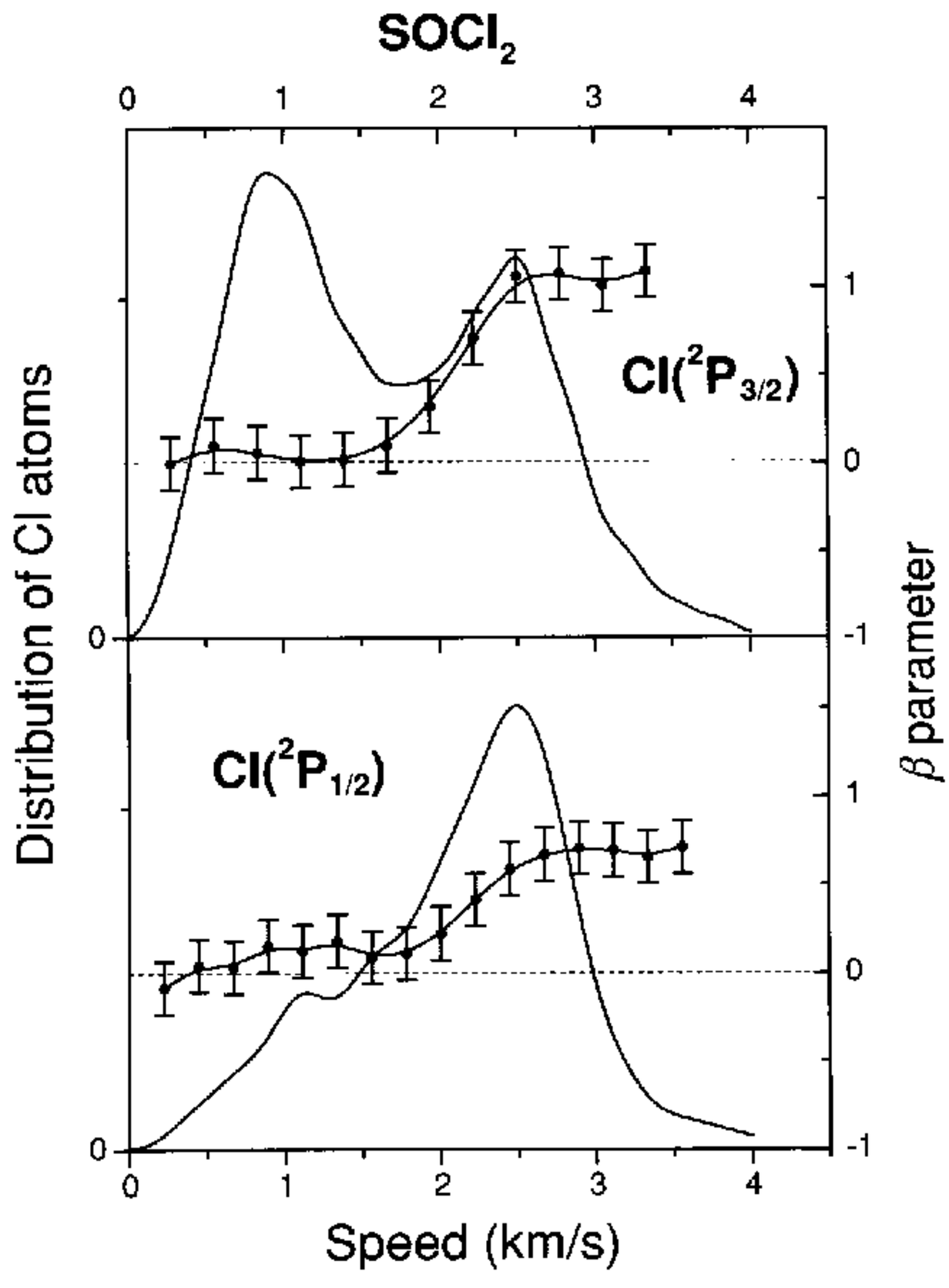

Fig. 6.16. Velocity distributions for the ground state $Cl(^2P_{3/2})$ and excited $Cl(^2P_{1/2})$ atoms in the photolysis of $SOCl_2$. The dependence of the β parameters on the Cl fragment velocity (right scale) are shown by curves with error bars.

in the second step, $SOCl^* \rightarrow SO + Cl$, described by an almost isotropic angular distribution of Cl atoms. Thus the three-body decay of $SOCl_2$ is asynchronously concerted or sequential, but not synchronously concerted.

6.6 The road ahead and concluding remarks

Three-dimensional photofragment imaging techniques have proved to be a powerful tool to study the velocity (speed and angle) distributions of the products of photodissociation processes. The progress is directly comparable with real 3-D (stereo) pictures relative to 2-D photos. It is hoped that the abundance of new experimental information available for this new method will stimulate future theoretical studies. Generally, the merits of this method lie in the investigation of photochemical processes where no cylindrical symmetry with respect to any axis is maintained,

covering all aspects of reactant and product alignment and orientation. Here, 3-D imaging allows the most direct measurements of the underlying effects, regardless of whether they are induced in the preparation of the sample or by the dynamics of the elementary reaction.

Further extensions of this method will probably go in two directions: first, there are coincidence measurements, that is, the simultaneous observation of two fragments resulting from photodissociation of a parent molecule. This technique must directly provide all three speed components of both the fragments. Of particular interest may be applications of this technique to study the photoinduced three-body dissociation ($ABC \rightarrow A + B + C$) since for these processes only a combination of 3-D imaging with coincidence measurements provides enough information for a complete kinematic analysis.

Other directions of future research may be the detailed study of speed distributions of the products of chemical reactions or from the photodissociation processes with vibrational preexcitation of the reactants.

Acknowledgements

We appreciate the great support of Dr. U. Titt and Dr. M. Roth. The authors A. Chichinin and T. Einfeld gratefully acknowledge the support of the Alexander von Humboldt Foundation and the Fonds der chemischen Industrie.

References

1. A. J. R. Heck, D. W. Chandler, *Ann. Rev. Phys. Chem.* **46**, 335–72 (1995).
2. V. Aquilanti, D. Ascenzi, M. de Castro Vítores, F. Pirani, D. Cappelletti, *J. Chem. Phys.* **111**, 2620–32 (1999).
3. F. Pirani, D. Cappelletti, M. Bartolomei, V. Aquilanti, M. Scotoni, M. Vescovi, *et al.*, *Phys. Rev. Lett.* **86**, 5035–8 (2001).
4. V. Aquilanti, D. Ascenzi, D. Cappelletti, F. Pirani, *Nature* **371**, 399–402 (1994).
5. V. Aquilanti, D. Ascenzi, D. Cappelletti, F. Pirani, *J. Phys. Chem.* **99**, 13620–6 (1995).
6. V. Aquilanti, D. Ascenzi, D. Cappelletti, R. Fedeli, F. Pirani, *J. Phys. Chem. A* **101**, 7648–56 (1997).
7. S. Harich, A. M. Wodtke, *J. Chem. Phys.* **107**, 5983–6 (1997).
8. E. B. Anthony, W. Schade, M. J. Bastian, V. M. Bierbaum, S. R. Leone, *J. Chem. Phys.* **106**, 5413–22 (1997).
9. D. P. de Bruijn, J. Los, *Rev. Sci. Instrum.* **53**, 1020–6 (1982).
10. J. C. Brenot, M. Durup-Ferguson. In: *State-Selected and State-to-State Ion-Molecule Reaction Dynamics*, Part 1: Experiment, ed. C. Y. Ng, M. Baer, (Wiley, New York, 1992), pp. 309–99.
11. H. Helm, P. C. Cosby, *J. Chem. Phys.* **86**, 6813–6822 (1987).
12. R. E. Continetti, D. R. Cyr, D. L. Osborn, D. J. Leahy, D. M. Neumark, *J. Chem. Phys.* **99**, 2616–31 (1993).
13. M. Takahashi, J. P. Cave, J. H. D. Eland, *Rev. Sci. Instrum.* **71**, 1337–44 (2000).

14. C. Maul, K.-H. Gericke, *Int. Rev. Phys. Chem.* **16**, 1–79 (1997).
15. C. Maul, K.-H. Gericke, *J. Phys. Chem. A* **104**, 2531–41 (2000).
16. J. Danielak, U. Domin, R. Kepa, M. Rytel, M. Zachwieja, *J. Mol. Spect.* **181**, 394–402 (1997).
17. D. R. Miller, In: *Atomic and Molecular Beam Methods* vol. 2, ed. G. Scoles, (Oxford University Press, New York, Oxford, 1992), pp. 14–53.
18. S. E. Sobottka, M. B. Williams, *IEEE Trans. Nucl. Sci.* **35**, 348–51 (1988).
19. O. Jagutzki, V. Mergel, K. Ullmann-Pfleger, L. Spielberger, U. Dörner, H. Schmidt-Böcking, *Nucl. Instrum. Methods A*, **447**, 244–9 (2002).
20. M. Lampton, O. Siegmund, R. Raffanti, *Rev. Sci. Instrum.* **58**, 2298–2305 (1987).
21. Z. Amitay, D. Zajfman, *Rev. Sci. Instrum.* **68**, 1387–92 (1997).
22. T. Ishiwata, A. Ishiguro, K. Obi, *J. Mol. Spectrosc.* **147**, 300–20 (1991).
23. Y. Matsumi, K. Tonokura, M. Kawasaki, *J. Chem. Phys.* **97**, 1065–71 (1992).
24. P. C. Samartzis, I. Sakellariou, T. Gougousi, T. N. Kitsopoulos, *J. Chem. Phys.* **107**, 43–8 (1997).
25. A. J. Alexander, Z. H. Kim, S. A. Kandel, R. N. Zare, T. P. Rakitzis, Y. Asano, S. Yabushita, *J. Chem. Phys.* **113**, 9022–31 (2000).
26. Y. Mo, T. Suzuki, *J. Chem. Phys.* **112**, 3463–73 (2000).
27. A. S. Bracker, E. R. Wouters, A. G. Suits, Y. T. Lee, O. S. Vasyutinskii, *Phys. Rev. Lett.* **80**, 1626–29 (1998).
28. A. S. Bracker, E. R. Wouters, A. G. Suits, O. S. Vasyutinskii, *J. Chem. Phys.* **110**, 6749–65 (1999).
29. K. O. Korovin, B. V. Picheyev, O. S. Vasyutinskii, H. Valipour, D. Zimmerman, *J. Chem. Phys.* **112**, 2059–62 (2000).
30. C.-H. Hsieh, Y.-S. Lee, A. Fujii, S.-H. Lee, K. P. Liu, *Chem. Phys. Lett.* **277**, 33–8 (1997).
31. D. J. Bamford, M. J. Dyer, W. K. Bischel, *Phys. Rev. A* **36**, 3497–3500 (1987).
32. C. Maul, T. Haas, K.-H. Gericke, F. J. Comes, *J. Chem. Phys.* **102**, 3238–47 (1995).
33. C. Maul, T. Haas, and K.-H. Gericke, *J. Phys. Chem. A* **101**, 6619–32 (1997).
34. S. Arepalli, N. Presser, D. Robie, R. J. Gordon, *Chem. Phys. Lett.* **118**, 88–92 (1985).